AIAA JOURNAL
Vol. 49, No. 2, February 2011

Dynamic Response of Highly Flexible Flying Wings

Weihua Su* and Carlos E. S. Cesnik†
University of Michigan, Ann Arbor, Michigan 48109-2140

DOI: 10.2514/1.J050496

This paper presents a method to model and analyze the coupled nonlinear flight dynamics and aeroelasticity of highly flexible flying wings. A low-order nonlinear strain-based finite element framework is used, which is capable of capturing the fundamental impact of geometrically nonlinear effects in a computationally effective formulation target for preliminary vehicle design and control evaluation. A simple model to capture the change in the wing torsional stiffness due to skin wrinkling arising from large bending curvatures is proposed. Finite-state unsteady subsonic aerodynamics with simplified stall models are incorporated to complete the aeroelastic representation of flying wings. In studying the flying wing dynamic response, a spatially and temporally distributed discrete gust model is introduced. With the proposed formulations, numerical studies are conducted based on a representative highly flexible flying wing subjected to finite disturbances.

Nomenclature

A_c	=	gust amplitude at center of region, m/s
A_E, A_N	=	spatial distribution functions of gust amplitude in east and north directions, respectively
a_0	=	local aerodynamic frame, with a_{0y} axis aligned with zero lift line of airfoil
a_1	=	local aerodynamic frame, with a_{1y} axis aligned with airfoil motion velocity
B	=	body reference frame
B^F, B^M	=	influence matrices for the distributed forces and moments
b	=	positions and orientations of the B frame, as time integral of β
b_c	=	semichord of airfoil, m
C_{FF}, C_{FB}, C_{BF}, C_{BB}	=	components of the generalized damping matrix
C^{GB}	=	rotation matrix from B frame to G frame
$c_{l_{\max}}$	=	maximum lift coefficient when stall angle is reached
$c_{l\alpha}$	=	lift curve slope
$c_{l\delta}$, $c_{m\delta}$	=	lift and moment slopes due to flap deflection
c_{m0}, c_{d0}	=	moment and drag coefficients for zero angle of attack
$c_{m0_{\text{stall}}}$	=	moment coefficient when stall angle is reached
d	=	distance of midchord in front of beam reference axis, m
F_1, F_2, F_3	=	influence matrices in inflow equations with independent variables
F^{dist}, F^{pt}	=	distributed and point forces
G	=	global (inertial) reference frame
g	=	gravity acceleration column vector, m/s^2
H_{hb}	=	matrix consisting of influence from the Jacobian J_{hb} and body angular velocities ω_B
h	=	absolute positions and rotations of beam nodes
J	=	Jacobian matrix
K_{FF}	=	components of the generalized stiffness matrix
l_{ac}, m_{ac}, d_{ac}	=	aerodynamic loads on an airfoil about its aerodynamic center
M, C, K	=	discrete mass, damping, and stiffness matrices of whole system
M_{FF}, M_{FB}, M_{BF}, M_{BB}	=	components of generalized mass matrix
M^{dist}, M^{pt}	=	distributed and point moments
N	=	influence matrix for gravity force
n_E, n_N	=	tuning parameters that determine spatial distribution of gust amplitude
P_B	=	inertia position of B frame, resolved in G frame
p_B, θ_B	=	position and orientation of B frame, as time integral of v_B and ω_B, respectively
p_w	=	position of w frame with respect to B frame
q	=	independent variables of equations of motion
R_B, R_F	=	rigid-body and flexible components of generalized load vector
r, η	=	polar coordinates that determine location of a point within the gust region
r_0	=	radius of gust region, m
s	=	beam curvilinear coordinate, m
t	=	time, s
t_g	=	gust duration, s
t_{sw}	=	time when threshold bending curvature is reached, s
v_B, ω_B	=	linear and angular velocities of B frame, resolved in B frame itself
W^{ext}, W^{int}	=	external and internal virtual work, respectively
w	=	local beam reference frame defined at each node along beam reference line
x_{sw}	=	system variables at time when threshold bending curvature is reached
$\dot{y}$, $\dot{z}$	=	airfoil translational velocity components resolved in a_0 frame, m/s
$\dot{\alpha}$	=	airfoil angular velocity about a_{0x} axis, rad/s
α_{stall}	=	stall angle, deg
β	=	body velocities, with translational and angular components, resolved in B frame
δ	=	trailing-edge flap deflection, rad
ε	=	total elastic strain vector of aircraft
ε_e	=	element elastic strain vector
ε_{sw}	=	strain vector when flat bending curvature reaches threshold value
ε^0	=	initial (prescribed) elastic strain vector
ζ	=	quaternions defining orientation of B frame
θ	=	rotations of beam nodes, rad
λ	=	inflow states, m/s
λ_0	=	inflow velocities, m/s

Presented as Paper 2006-1636 at the 47th AIAA/ASME/ASCE/AHS/ASC Structures, Structural Dynamics, and Materials Conference, Newport, RI, 1–4 May 2006; received 17 February 2010; revision received 19 October 2010; accepted for publication 28 October 2010.

*Postdoctoral Research Fellow, Department of Aerospace Engineering; suw@umich.edu. Senior Member AIAA.

†Professor, Department of Aerospace Engineering; cesnik@umich.edu. Associate Fellow AIAA.

ρ = air density, kg/m^3
$\Omega_\zeta(\beta)$ = coefficient matrix of quaternion equations, a function of body angular velocities

Subscripts

B = reference to B frame
BB, BF = components of a matrix with respect to body/flexible differential equations of motion
F = reference to flexible degrees of freedom
FB, FF = components of a matrix with respect to flexible/body differential equations of motion
hb = h vector with respect to motion of B frame
$h\varepsilon$ = h vector with respect to strain ε
pb = nodal position with respect to motion of B frame
$p\varepsilon$ = nodal position with respect to strain ε
θb = nodal rotation with respect to motion of B frame
$\theta\varepsilon$ = nodal rotation with respect to strain ε

I. Introduction

HIGHLY flexible flying wings have been considered an important concept for high-altitude long-endurance (HALE) unmanned aerial vehicles (UAVs). In 1994, NASA initiated the Environmental Research Aircraft and Sensor Technology program, aimed at developing UAVs capable of long-duration and very high-altitude flights for atmospheric research. Under this program, an evolutionary series of unmanned aircraft: Pathfinder, Pathfinder Plus, Centurion, and Helios Prototype, were developed by AeroVironment, Inc. These HALE vehicles feature light wings with high aspect ratios, as illustrated in Fig. 1. The long and slender wings, by their inherent nature, can maximize the lift-to-drag ratio. On the other hand, these wings may undergo large deformations during normal operating loads, exhibiting geometrically nonlinear behavior. Because of this inherently high flexibility, traditional linear theories do not provide accurate estimations on HALE aircraft aeroelastic characteristics. Patil et al. [1,2] studied the aeroelasticity and flight dynamics of a HALE aircraft. The results indicated that the aeroelastic behavior and flight dynamic characteristic of the aircraft can be significantly changed due to the large deflection of the flexible wings. This leads to the conclusion that the coupled effects between the large deflection due to the vehicle flexibility and the flight dynamics, as well as other aeroelastic effects (e.g., gust response and flutter instability) must be properly accounted for in a nonlinear aeroelastic framework. Under certain operating conditions when the aircraft's deformed shape is significantly different from its undeformed one, the aeroelastic analysis must be based on the actual trimmed conditions.

Fig. 1 Helios Prototype as a sample of highly flexible flying wing (photo courtesy of NASA Dryden Flight Research Center).

Recently, there has been increasing interest in the analysis of the dynamic response of highly flexible flying wing vehicles. The trigger was the loss of the Helios Prototype (HP03) [3], which indicated that these long, slender flying wing vehicles can be very sensitive to disturbance. The number one recommendation from the NASA investigation panel was [3] "(to) develop more advanced, multidisciplinary (structures, aeroelastic, aerodynamics, atmospheric, materials, propulsion, controls, etc.) 'time-domain' analysis methods appropriate to highly flexible, 'morphing' vehicles."

Patil and Hodges [4] have studied the flight dynamics of a flying wing vehicle that resembles the Helios Prototype. Because of the high flexibility of the configuration, the vehicle undergoes large deformation at its trimmed condition when fully loaded. According to their study, the flight dynamic characteristics of the deformed vehicle under heavy payload conditions present an unstable phugoid mode. The classical short-period mode does not exist. In that work, the nonlinear time-marching simulation was performed with no stall effects and no simulation other than the response to the aileron perturbation was presented.

Gust responses of highly flexible flying wings have become a focus of research. Gusts are random in nature. They can affect different aspects of the aircraft's operation, such as its dynamic load, flight stability and safety, and control [5]. In a high-fidelity analysis, a random gust is represented by a continuous model. However, discrete gust models are also used due to their simplicity (also mandated by Federal Aviation Regulations). Patil and Taylor [6] performed frequency-domain analysis of linear gust responses of a highly flexible flying wing, where the spanwise nonuniform gust excitations of the highly flexible vehicle led to larger deformations than the uniform one. That work was extended to the time domain in [7], where a gust input time series was first created based on the assumed gust power spectral density. The response stochastic parameters were calculated from the response time series. This method could be applied in the time domain for analysis of nonlinear gust responses.

Another important characteristic of the long and slender wings relates to their natural frequencies. These wings tend to have very low-frequency elastic modes that may interact with the rigid-body motion of the aircraft, which makes it necessary to analyze the nonlinear aeroelasticity of the whole vehicle within a coupled formulation. Love et al. [8] studied the body-freedom flutter of a high-aspect-ratio flying wing model. Their results indicated that the body-freedom flutter was critical for lower altitude portions of the flight envelope and that active flutter suppression should be considered. Raghavan and Patil [9] conducted coupled aeroelastic and flight dynamic studies of a highly flexible flying wing. They identified that the large wing deformation under operating conditions might change the flight dynamic behavior. Shearer and Cesnik [10] demonstrated that vehicle trajectories calculated from nonlinear rigid-body and linearized solutions might significantly differ from the ones based on fully nonlinear solutions for highly flexible aircraft. Therefore, fully nonlinear simulations may be necessary to properly predict the vehicle trajectories.

While few efforts can be found in the literature that attempt to address the response of a highly flexible flying wing considering different nonlinear effects, its dynamic response is still an open problem. As already established, highly flexible flying wings will present large (nonlinear) deformations under the operating loads, which come with a large local angle of attack and dihedral angle. This large dihedral angle may cause vehicle instability under disturbances or gust loads. One particular aspect that can potentially bring some interesting nonlinear effects is associated with the wrinkling of the wing skin. To achieve very light constructions, the typical wing structure of such vehicles is composed of a main (circular) spar with ribs attached to it along specific span stations. A very light and thin film is used to close the airfoil and provide the desired airfoil shape. The resulting structure can be represented by a closed cell beam section. Significant torsional stiffness comes from the presence of the skin. However, during large bending deformations, the skin may unstretch and wrinkle. The local torsional stiffness will drop as a result of the skin wrinkling. Once the bending curvature is reduced, the skin stretches again and the original configuration may be

recovered. This additional nonlinear effect can alter the vehicle aeroelastic response during flight. A bilinear stiffness model may be used to capture such effects. Dynamic aeroelastic response of multi-segmented hinged wings was originally studied theoretically and experimentally by Radcliffe and Cesnik [11]. The multihinged wings present a nonlinear (bilinear) stiffness. In their study, a method of modeling the aeroelastic characteristics of multihinged wings was proposed and could be adapted for the very flexible wing problem discussed here. The Hénon method [12] was used to switch between bilinear states of the wing in bending.

This paper presents the formulation and modeling of the coupled nonlinear flight dynamics and aeroelasticity of highly flexible flying wings. It extends the University of Michigan's Nonlinear Aeroelastic Simulation Toolbox (UM/NAST) [10,13,14] with a spatially and temporally distributed gust model and a local bilinear torsional stiffness representation of the skin wrinkling due to wing bending deformations. The formulation is then applied to a Helios-like vehicle [4], and different aeroelastic responses are studied.

II. Theoretical Formulation

Because of the interaction between flight dynamics and aeroelastic response, the formulation includes six rigid-body and multiple flexible degrees of freedom. The structural members are allowed fully coupled three-dimensional bending, twisting, and extensional deformations. Control surfaces are included for maneuver studies. A finite-state unsteady aerodynamic model is integrated into the system equations. An overview of the formulation implemented in UM/NAST is described next. Particular emphasis is given to the two main additions to the simulation framework that are explored in this paper: 1) spatially and temporally distributed discrete gust model, and 2) bilinear torsional stiffness model.

A. Fundamental Description

As shown in Fig. 2, a global (inertial) frame G is defined, which is fixed on the ground. A body frame B is built in the global frame to describe the vehicle position and orientation, with B_x pointing to the right wing, B_y pointing forward, and B_z being the cross product of B_x and B_y. The position and orientation b and the time derivatives $\dot{b}$ and $\ddot{b}$ of the B frame can be defined as

$$b = \begin{Bmatrix} p_B \\ \theta_B \end{Bmatrix}, \qquad \dot{b} = \beta = \begin{Bmatrix} \dot{p}_B \\ \dot{\theta}_B \end{Bmatrix} = \begin{Bmatrix} v_B \\ \omega_B \end{Bmatrix}$$
$$\ddot{b} = \dot{\beta} = \begin{Bmatrix} \ddot{p}_B \\ \dot{\theta}_B \end{Bmatrix} = \begin{Bmatrix} \dot{v}_B \\ \dot{\omega}_B \end{Bmatrix} \tag{1}$$

where p_B and θ_B are body position and orientation, both resolved in the body frame B. Note that the origin of the body frame is arbitrary in the vehicle, and it does not have to be the location of the vehicle's center of gravity.

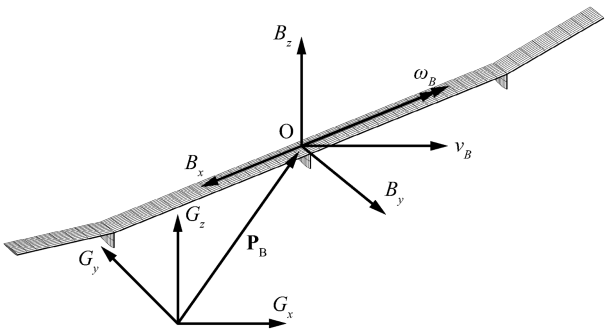

Fig. 2 Global and body reference frames.

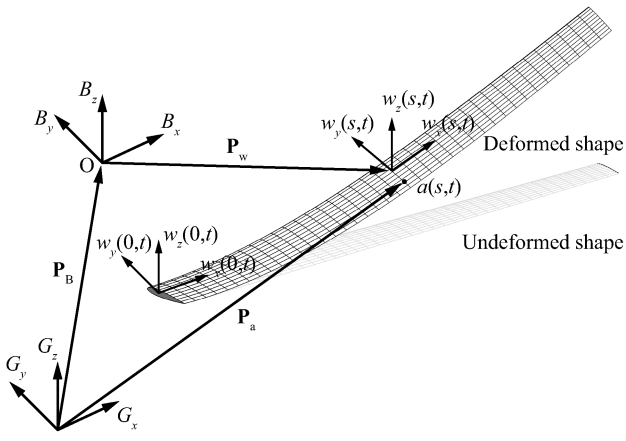

Fig. 3 Flexible lifting-surface frames and body reference frame.

As described in Fig. 3, a local beam frame w is built within the body frame, which is used to define the position and orientation of each node along the beam reference line. Vectors w_x, w_y, and w_z are bases of the beam frame, for which the directions are pointing along the beam reference axis, toward the leading edge, and normal to the beam surface, respectively, resolved in the body frame.

To model the elastic deformation of slender beams, a nonlinear beam element was developed in [13,15]. Each of the elements has three nodes and four local strain degrees of freedom, denoted as

$$\varepsilon_e^T = \{\, \varepsilon_x^T, \quad \kappa_x^T, \quad \kappa_y^T, \quad \kappa_z^T \,\} \tag{2}$$

where ε_x is the extensional strain, κ_x is the twist of the beam reference line, and κ_y and κ_z are the bending about local w_y and w_z axes, respectively. The total strain vector of the complete aircraft is obtained by stacking the element strain vectors:

$$\varepsilon^T = \{\, \varepsilon_{e1}^T, \quad \varepsilon_{e2}^T, \quad \varepsilon_{e3}^T, \quad \cdots \,\} \tag{3}$$

With the rigid-body and elastic degrees of freedom defined, the complete independent set of variables of the strain-based formulation is

$$q = \begin{Bmatrix} \varepsilon \\ b \end{Bmatrix} = \begin{Bmatrix} \varepsilon \\ p_B \\ \theta_B \end{Bmatrix}, \qquad \dot{q} = \begin{Bmatrix} \dot{\varepsilon} \\ \dot{\beta} \end{Bmatrix} = \begin{Bmatrix} \dot{\varepsilon} \\ v_B \\ \omega_B \end{Bmatrix}$$
$$\ddot{q} = \begin{Bmatrix} \ddot{\varepsilon} \\ \dot{\beta} \end{Bmatrix} = \begin{Bmatrix} \ddot{\varepsilon} \\ \dot{v}_B \\ \dot{\omega}_B \end{Bmatrix} \tag{4}$$

The position and orientation of each node along the beam are defined by a vector consisting of 12 components, denoted as

$$h(s)^T = \{\, [p_B + p_w(s)]^T, \quad w_x(s)^T, \quad w_y(s)^T, \quad w_z(s)^T \,\} \tag{5}$$

where p_w is the position of the w frame resolved in the body frame. The derivatives and variations of the dependent variable h are related with those of the independent ones as

$$\begin{aligned} \delta h &= J_{h\varepsilon}\delta\varepsilon + J_{hb}\delta b, & \dot{h} &= J_{h\varepsilon}\dot{\varepsilon} + J_{hb}\dot{b} = J_{h\varepsilon}\dot{\varepsilon} + J_{hb}\beta \\ dh &= J_{h\varepsilon}d\varepsilon + J_{hb}db, & \ddot{h} &= J_{h\varepsilon}\ddot{\varepsilon} + \dot{J}_{h\varepsilon}\dot{\varepsilon} + J_{hb}\dot{\beta} + \dot{J}_{hb}\beta \end{aligned} \tag{6}$$

where

$$J_{h\varepsilon} \equiv \frac{\partial h}{\partial \varepsilon}, \qquad J_{hb} \equiv \frac{\partial h}{\partial b} \tag{7}$$

are transformation Jacobians obtained from kinematics. The other necessary Jacobian matrices, including $J_{p\varepsilon}$, $J_{\theta\varepsilon}$, J_{pb}, and $J_{\theta b}$, which relate the nodal positions and rotations to the independent variables, can be derived from $J_{h\varepsilon}$ and J_{hb} [10,13,14].

B. Elastic Equations of Motion

The elastic equations of motion are derived by following the principle of virtual work. The virtual work of an elastic wing consists of the contributions of inertia forces, internal strains and strain rates,

and external loads. The contribution of each virtual work is derived separately and then summed at the end to represent the total virtual work of the complete vehicle. This paper gives a brief overview of it, and the detailed derivation process can be found in [16]. The virtual work due to internal and external loads is given as

$$\begin{aligned}\delta W^{\text{int}} &= -\delta h^T M\ddot{h} - \delta h^T M H_{hb}\beta - \delta h^T M\dot{J}_{hb}\beta - \delta\varepsilon^T C\dot{\varepsilon} \\ &\quad - \delta\varepsilon^T K(\varepsilon - \varepsilon^0) \\ \delta W^{\text{ext}} &= -\delta h^T N g + \delta p_w^T B^F F^{\text{dist}} + \delta\theta^T B^M M^{\text{dist}} + \delta p_w^T F^{pt} \\ &\quad + \delta\theta^T M^{\text{pt}}\end{aligned} \tag{8}$$

The dependent variables (h, p_w, and θ) can be replaced by the independent variable by applying the Jacobians [see Eq. (6)] and their subsets. Therefore, the total virtual work on a beam can be written as

$$\begin{aligned}\delta W &= \delta W^{\text{int}} + \delta W^{\text{ext}} \\ &= -\{\delta\varepsilon^T \quad \delta b^T\}\left(\begin{bmatrix} J_{h\varepsilon}^T M J_{h\varepsilon} & J_{h\varepsilon}^T M J_{hb} \\ J_{hb}^T M J_{h\varepsilon} & J_{hb}^T M J_{hb}\end{bmatrix}\begin{Bmatrix}\ddot{\varepsilon}\\ \dot{\beta}\end{Bmatrix}\right. \\ &\quad + \begin{bmatrix} J_{h\varepsilon}^T M\dot{J}_{h\varepsilon} & 0 \\ J_{hb}^T M\dot{J}_{h\varepsilon} & 0\end{bmatrix}\begin{Bmatrix}\dot{\varepsilon}\\ \beta\end{Bmatrix} + \begin{bmatrix} 0 & J_{h\varepsilon}^T M H_{hb} \\ 0 & J_{hb}^T M H_{hb}\end{bmatrix}\begin{Bmatrix}\dot{\varepsilon}\\ \beta\end{Bmatrix} \\ &\quad + \begin{bmatrix} 0 & 2J_{h\varepsilon}^T M\dot{J}_{hb} \\ 0 & 2J_{hb}^T M\dot{J}_{hb}\end{bmatrix}\begin{Bmatrix}\dot{\varepsilon}\\ \beta\end{Bmatrix} + \begin{bmatrix} C & 0 \\ 0 & 0\end{bmatrix}\begin{Bmatrix}\dot{\varepsilon}\\ \beta\end{Bmatrix} \\ &\quad \left. + \begin{bmatrix} K & 0 \\ 0 & 0\end{bmatrix}\begin{Bmatrix}\varepsilon\\ b\end{Bmatrix} - \begin{Bmatrix} K\varepsilon^0 \\ 0\end{Bmatrix}\right) + \{\delta\varepsilon^T \quad \delta b^T\}\left(-\begin{bmatrix} J_{h\varepsilon}^T \\ J_{hb}^T\end{bmatrix} N g\right. \\ &\quad + \begin{bmatrix} J_{p\varepsilon}^T \\ J_{pb}^T\end{bmatrix} B^F F^{\text{dist}} + \begin{bmatrix} J_{\theta\varepsilon}^T \\ J_{\theta b}^T\end{bmatrix} B^M M^{\text{dist}} + \begin{bmatrix} J_{p\varepsilon}^T \\ J_{pb}^T\end{bmatrix} F^{\text{pt}} \\ &\quad \left. + \begin{bmatrix} J_{\theta\varepsilon}^T \\ J_{\theta b}^T\end{bmatrix} M^{\text{pt}}\right)\end{aligned} \tag{9}$$

Following the same process described in [16], the elastic system equations of motion are eventually derived as

$$\begin{bmatrix} M_{FF} & M_{FB} \\ M_{BF} & M_{BB}\end{bmatrix}\begin{Bmatrix}\ddot{\varepsilon}\\ \dot{\beta}\end{Bmatrix} + \begin{bmatrix} C_{FF} & C_{FB} \\ C_{BF} & C_{BB}\end{bmatrix}\begin{Bmatrix}\dot{\varepsilon}\\ \beta\end{Bmatrix} + \begin{bmatrix} K_{FF} & 0 \\ 0 & 0\end{bmatrix}\begin{Bmatrix}\varepsilon\\ b\end{Bmatrix} = \begin{Bmatrix} R_F \\ R_B\end{Bmatrix} \tag{10}$$

where the generalized inertia, damping, and stiffness matrices are

$$\begin{aligned} &M_{FF}(\varepsilon) = J_{h\varepsilon}^T M J_{h\varepsilon}, \qquad M_{FB}(\varepsilon) = J_{h\varepsilon}^T M J_{hb}, \\ &M_{BF}(\varepsilon) = J_{hb}^T M J_{h\varepsilon}, \qquad M_{BB}(\varepsilon) = J_{hb}^T M J_{hb}, \\ &C_{FF}(\varepsilon,\dot{\varepsilon},\beta) = C + J_{h\varepsilon}^T M\dot{J}_{h\varepsilon}, \\ &C_{FB}(\varepsilon,\dot{\varepsilon},\beta) = J_{h\varepsilon}^T M H_{hb} + 2J_{h\varepsilon}^T M\dot{J}_{hb}, \\ &C_{BF}(\varepsilon,\dot{\varepsilon},\beta) = J_{hb}^T M\dot{J}_{h\varepsilon}, \\ &C_{BB}(\varepsilon,\dot{\varepsilon},\beta) = J_{hb}^T M H_{hb} + 2J_{hb}^T M\dot{J}_{hb}, \qquad K_{FF} = K\end{aligned} \tag{11}$$

and the generalized force vector is

$$\begin{aligned}\begin{Bmatrix} R_F \\ R_B\end{Bmatrix} &= \begin{Bmatrix} K_{FF}\varepsilon^0 \\ 0\end{Bmatrix} - \begin{bmatrix} J_{h\varepsilon}^T \\ J_{hb}^T\end{bmatrix} N g + \begin{bmatrix} J_{p\varepsilon}^T \\ J_{pb}^T\end{bmatrix} B^F F^{\text{dist}} \\ &\quad + \begin{bmatrix} J_{\theta\varepsilon}^T \\ J_{\theta b}^T\end{bmatrix} B^M M^{\text{dist}} + \begin{bmatrix} J_{p\varepsilon}^T \\ J_{pb}^T\end{bmatrix} F^{\text{pt}} + \begin{bmatrix} J_{\theta\varepsilon}^T \\ J_{\theta b}^T\end{bmatrix} M^{\text{pt}}\end{aligned} \tag{12}$$

where N, B^F, and B^M are the influence matrices for the gravity force, distributed forces, and distributed moments, respectively, which come from the numerical integration. The generalized force vector involves the effects from initial strains ε^0, gravity fields g, distributed forces F^{dist}, distributed moments M^{dist}, point forces F^{pt}, and point moments M^{pt}. The aerodynamic forces and moments are considered as distributed loads.

C. Unsteady Aerodynamics

The distributed loads, F^{dist} and M^{dist} in Eq. (12), are divided into aerodynamic loads and user-supplied loads. The unsteady aerodynamic loads used in the current study are based on the two-dimensional (2-D) finite-state inflow theory, provided in [17]. The theory calculates aerodynamic loads on a thin airfoil section undergoing large motions in an incompressible inviscid subsonic flow. Based on known aerodynamic coefficients, the lift, moment, and drag of a thin 2-D airfoil section about its aerodynamic center are given by

$$\begin{aligned} l_{\text{ac}} &= \pi\rho b_c^2(-\ddot{z} + \dot{y}\dot{\alpha} - d\ddot{\alpha}) + c_{l\alpha}\rho b_c\dot{y}^2\left[-\frac{\dot{z}}{\dot{y}} + \left(\frac{1}{2}b_c - d\right)\frac{\dot{\alpha}}{\dot{y}}\right. \\ &\quad \left. - \frac{\lambda_0}{\dot{y}}\right] + \rho b_c\dot{y}^2 c_{l\delta}\delta \\ m_{\text{ac}} &= \pi\rho b_c^3\left[\frac{1}{2}\ddot{z} - \dot{y}\dot{\alpha} - \left(\frac{1}{8}b_c - \frac{1}{2}d\right)\ddot{\alpha}\right] + 2\rho b_c^2\dot{y}^2(c_{m0} + c_{m\delta}\delta) \\ d_{\text{ac}} &= -\rho b_c\dot{y}^2 c_{d0}\end{aligned} \tag{13}$$

where δ is the trailing-edge flap deflection angle, b_c is the semichord, d is the distance of the midchord in front of the reference axis, $c_{l\alpha}$ is the lift curve slope, $c_{l\delta}$ and $c_{m\delta}$ are the lift and moment slopes due to flap deflection, respectively, and c_{d0} and c_{m0} are the drag and moment coefficients for zero angle of attack, respectively. The quantity $-\dot{z}/\dot{y}$ is the angle of attack that consists of the contribution from both the pitching angle and the unsteady plunging motion of the airfoil. The different velocity components are shown in Fig. 4. The inflow parameter λ_0 counts for induced flow due to free vorticity, which is the summation of the inflow states λ, as described in [17] and given by

$$\dot{\lambda} = F_1\ddot{q} + F_2\dot{q} + F_3\lambda = F_1\begin{Bmatrix}\ddot{\varepsilon}\\ \dot{\beta}\end{Bmatrix} + F_2\begin{Bmatrix}\dot{\varepsilon}\\ \beta\end{Bmatrix} + F_3\lambda \tag{14}$$

Note that the finite-span corrections are also included in the force distribution and may come from a CFD solution of the problem or experimental data if available. The aerodynamic loads about the aerodynamic center will be transferred to the wing elastic axis and rotated into the body frame for the solution of equations of motion.

D. Simplified Stall Models

There are two stall models considered in the current study. For stall model 1, the lift coefficient c_l is kept constant and equal to $c_{l_{\max}}$ once the angle of attack goes beyond the stall angle, and the moment coefficient c_{m0} remains the same as before stall. Stall model 2 is similar to stall model 1, with the only difference that, now, the moment coefficient is dropped to another constant value of $c_{m0_{\text{stall}}}$, as illustrated in Figs. 5 and 6.

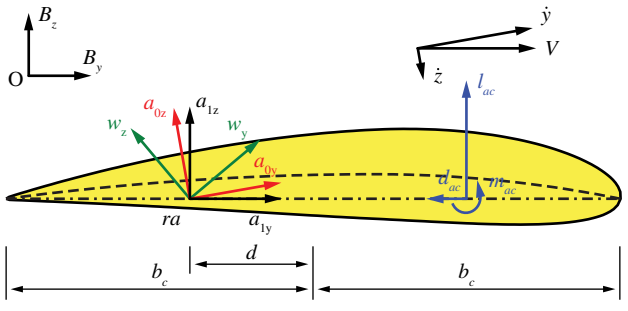

Fig. 4 Airfoil coordinate system and velocity components.

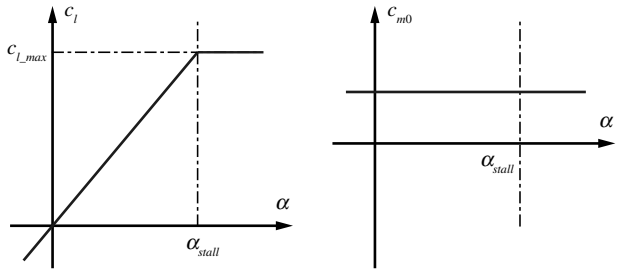

a) Lift coefficient **b) Moment coefficient**

Fig. 5 Variation of lift and moment coefficients for stall model 1.

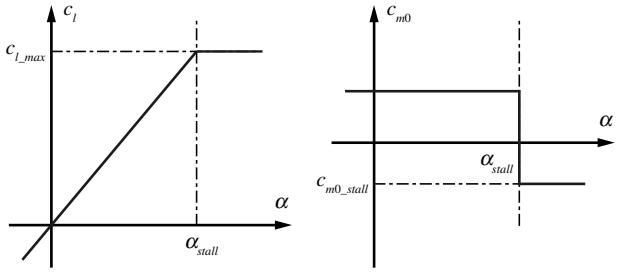

a) Lift coefficient **b) Moment coefficient**

Fig. 6 Variation of lift and moment coefficients for stall model 2.

E. Discrete Gust Model

In general, gust disturbance is stochastic. In the current work, the gust model is simplified as an elliptical region with only vertical disturbance. However, this gust model is both space and time dependent. The gust region is located on the flight path of the vehicle. At each time, the amplitude of gust speed reaches the maximum at the center and reduces to zero at the boundary. Figure 7 shows the amplitude distribution of the gust model. For the particular example used in the current study, the gust region is defined as a circular one. The amplitude distributions along the north and east directions may be different. At each location within the gust region, the amplitudes follow the same temporal variation. The basic equations governing the gust model are

$$A(r,\eta,t)=\frac{1}{2}A_c\left[1-\cos\left(2\pi\frac{t}{t_g}\right)\right]\sqrt{(A_E\cos\eta)^2+(A_N\sin\eta)^2} \quad (15)$$

$$\begin{aligned} A_E(r) &= \sin\left(\frac{\pi}{2}\left[1-\left(\frac{r}{r_0}\right)^{n_E}\right]\right), \\ A_N(r) &= \sin\left(\frac{\pi}{2}\left[1-\left(\frac{r}{r_0}\right)^{n_N}\right]\right), \qquad 0<r\le r_0 \end{aligned} \quad (16)$$

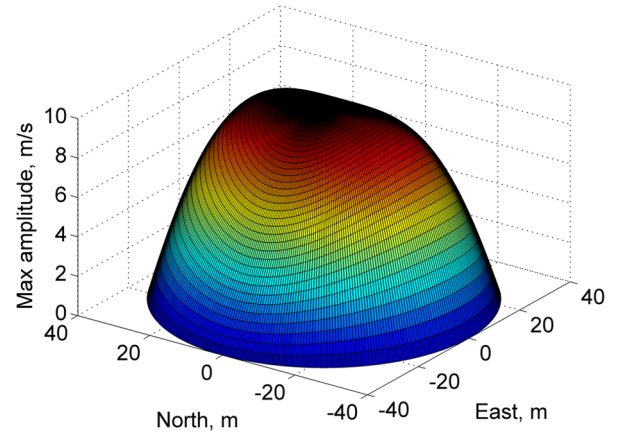

Fig. 7 Example of gust spatial distribution for $n_E = 1$, $n_N = 2$, and $A_c = 10$ m/s.

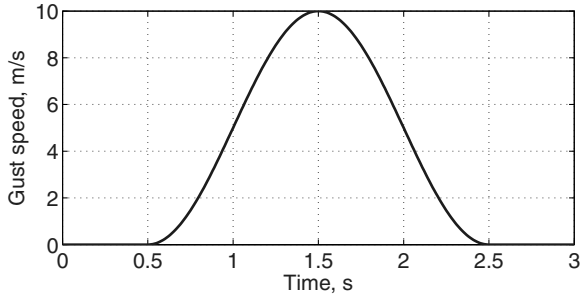

Fig. 8 Time variation of the gust speed.

where footnotes E and N stand for east and north directions, respectively. A_c is the gust amplitude at the center of region, r_0 is the outer radius of the gust region, r is the distance from one point within the gust region to the gust center, η is the orientation angle of the point with respect to the east direction, and n_E and n_N are parameters used for adjusting the gust spatial distribution along the east and north directions, respectively. By choosing different n_E and n_N, the spatial variation of gust amplitudes in the east and north directions will be different. It also satisfies the requirement that the amplitude at the gust center is the maximum and decreased down to zero at the boundary. The spatial distribution is then combined with the one-minus-cosine time distribution, leading to the gust model represented by Eq. (15). Finally, t_g is the gust duration. Figure 8 shows the one-minus-cosine time variation of the amplitude at the gust center. Different temporal variations can be applied for numerical studies.

F. Coupled Nonlinear Aeroelastic and Flight Dynamic System Equations of Motion

The coupled nonlinear aeroelastic and flight dynamic system equations of motion are obtained by augmenting the equations of rigid-body motion and elastic deformations with the inflow equations, which can be represented as

$$\begin{aligned} &\begin{bmatrix} M_{FF}(\varepsilon) & M_{FB}(\varepsilon) \\ M_{BF}(\varepsilon) & M_{BB}(\varepsilon) \end{bmatrix}\begin{Bmatrix} \ddot{\varepsilon} \\ \dot{\beta} \end{Bmatrix}+\begin{bmatrix} C_{FF}(\dot{\varepsilon},\varepsilon,\beta) & C_{FB}(\dot{\varepsilon},\varepsilon,\beta) \\ C_{BF}(\dot{\varepsilon},\varepsilon,\beta) & C_{BB}(\dot{\varepsilon},\varepsilon,\beta) \end{bmatrix}\begin{Bmatrix} \dot{\varepsilon} \\ \beta \end{Bmatrix} \\ &+\begin{bmatrix} K_{FF} & 0 \\ 0 & 0 \end{bmatrix}\begin{Bmatrix} \varepsilon \\ b \end{Bmatrix}=\begin{Bmatrix} R_F(\ddot{\varepsilon},\dot{\varepsilon},\varepsilon,\dot{\beta},\beta,\lambda,\zeta) \\ R_B(\ddot{\varepsilon},\dot{\varepsilon},\varepsilon,\dot{\beta},\beta,\lambda,\zeta) \end{Bmatrix} \\ &\dot{\zeta}=-\frac{1}{2}\Omega_\zeta(\beta)\zeta, \quad \dot{P}_B=[C^{GB}(\zeta)\ \ 0]\beta, \\ &\dot{\lambda}=F_1\begin{Bmatrix} \ddot{\varepsilon} \\ \dot{\beta} \end{Bmatrix}+F_2\begin{Bmatrix} \dot{\varepsilon} \\ \beta \end{Bmatrix}+F_3\lambda \end{aligned} \quad (17)$$

where ζ are the quaternions describing the orientation of the body frame B, P_B is the inertial position of the B frame, and C^{GB} is the rotation matrix from the body frame to the global frame G [10].

G. Modeling of Skin Wrinkling

As discussed, for a typical highly flexible flying wing construction, significant torsional stiffness comes from the presence of the stretched thin skin. During large bending deformations, the skin may wrinkle. The unstretched skin causes the local torsional stiffness

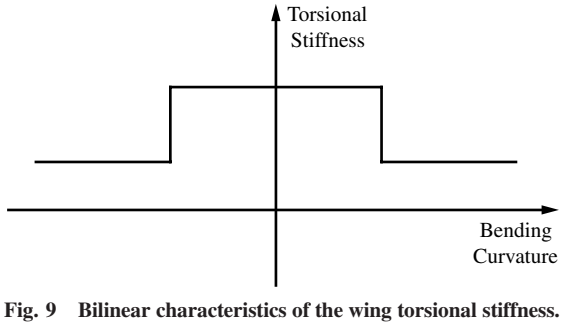

Fig. 9 Bilinear characteristics of the wing torsional stiffness.

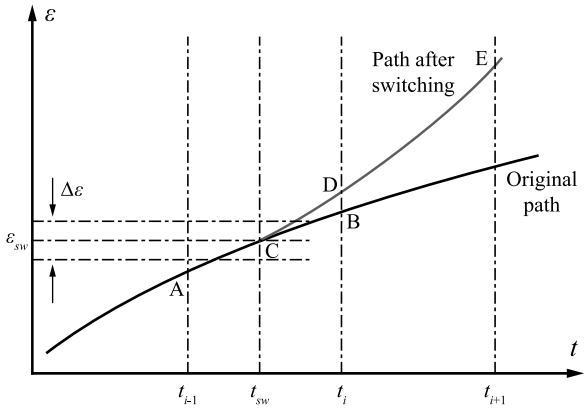

Fig. 10 Switching of system properties during time integration.

to drop. When the bending deformation is reduced and the wing skin is stretched again, the torsional stiffness is recovered. This effect is represented with a bilinear response, as shown in Fig. 9. To model it, a switch is set up such that, once the bending curvature increases to a predefined threshold value, the torsional stiffness is reduced. However, this reduction is not permanent. When the bending curvature falls back to being smaller than that threshold, the original torsional stiffness is recovered.

The most important issue for the modeling of this bilinear stiffness is to search for the time when the state (bending curvature) reaches the critical value (threshold value), which is denoted in Fig. 10 as t_{sw}. Hénon [12] proposed a method to determine the exact time when the threshold is reached and the corresponding value of all states at that point. It has been used in previous work [11] successfully. However, its implementation within the current work was shown to be difficult. Although the threshold strain could be determined accurately, threshold strain rates had unreasonable estimates.

An alternate approach adopted for the current study is based on linear interpolation. Suppose the threshold happens between t_{i-1} and t_i. The switching time can be estimated by using the following equations:

$$t_{sw} = \frac{\varepsilon_{sw} - \varepsilon_{i-1}}{0.5(\dot{\varepsilon}_{i-1} + \dot{\varepsilon}_i)} \tag{18}$$

$$x_{sw} = x_{i-1} + \frac{t_{sw} - t_{i-1}}{t_i - t_{i-1}}(x_i - x_{i-1}) \tag{19}$$

Equation (18) can give good approximation as long as the time step for integration is small enough. In practice, t_{sw} can be approximated by looking for the time point when the strain falls into a band of tolerance $\Delta\varepsilon$. However, this approach gives no information on the accuracy of the approximated x_{sw}, since the states obtained at t_{sw} are all based on the linear interpolation. To solve this problem, instead of using Eq. (19) directly, one step of time integration from t_{i-1} to t_{sw} can be performed to obtain the real states at t_{sw} and to ensure the approximation falls into an acceptable tolerance band.

III. Numerical Studies

To study the nonlinear characteristics of flying wings, a baseline flying wing aircraft is introduced. It is based directly on the vehicle definition presented in [4]. The vehicle performs level flight at sea level with a speed of 12.2 m/s. It is trimmed for equilibrium in horizontal flight at the given flight condition with different payloads. First, the model used here is compared with the one presented in [4]. Then, gust response, with and without stall effects, and skin wrinkling are studied for this vehicle concept.

A. Geometry

Figure 11 shows the geometry of the flying wing vehicle. It has a span of 72.8 m and a constant chord length of 2.44 m. The outboard one-third of the wing semispan has a dihedral angle of 10 deg. Wing

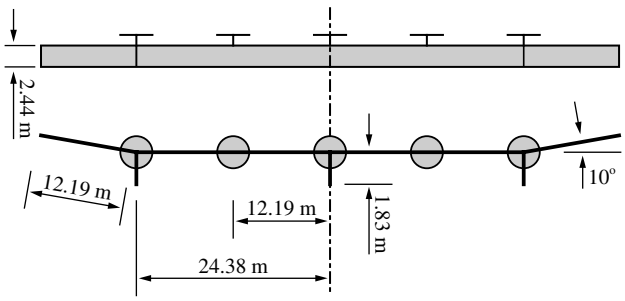

Fig. 11 Geometry of the flying wing model (after [4]).

cross-sectional properties can be found in Table 1. As indicated in Fig. 11, there are five propulsive units and three pods, which are located at the middle span and at two-thirds of the semispan at each side, respectively. The side pods have a mass of 22.70 kg each, and the center one has a mass of 27.23 kg. The payload is applied on the center pod, ranging from 0 (light) to 227 kg (heavy).

B. Trim Results

With the flight speed of 12.2 m/s at sea level, the flying wing vehicle is trimmed for equivalent lift and weight, equivalent thrust and drag, and zero pitching moment about the center of gravity of the aircraft. Flaplike control surfaces along the trailing edge and the engine thrusts are used as trim inputs. The payload is varied so that the vehicle mass is varied from light to heavy, as defined previously. The trim results are shown in Fig. 12 and Table 2, and the deformations at trim conditions of light and heavy configurations are graphically represented in Figs. 13 and 14, respectively. The results indicate that the static characteristics of the flying wing model used here are very similar to the ones in [4]. Note that, to achieve such correlation, the model in UM/NAST does not include either induced drag or drag associated with the deformation of the control surfaces. Therefore, the trim thrust does not vary with payload, as indicated in Table 2.

C. Stability Analysis of the Flying Wing Vehicle

To assess the flight stability of the flying wing vehicle with different payloads, a linearization of the aeroelastic equations of motion is performed at each trimmed condition, where the flight speed is 12.2 m/s at sea level. The nonlinear matrices in Eq. (17) are expanded with respect to the independent variables about each nonlinear equilibrium state. The resulting terms with the same

Table 1 Vehicle cross-sectional properties (after [4])

Parameter	Value
Elastic (reference) axis	25% chord
Center of gravity	25% chord
Stiffness properties	
Torsional rigidity	1.65×10^5 N · m^2
Flatwise bending rigidity	1.03×10^6 N · m^2
Chordwise bending rigidity	1.24×10^7 N · m^2
Inertia properties	
Mass per unit length	8.93 kg/m
Mass moment of inertia (torsional)	4.15 kg · m
Mass moment of inertia (flatwise Bend)	0.69 kg · m
Mass moment of inertia (chordwise Bend)	3.46 kg · m
Aerodynamic coefficients for wings (about 25% chord)	
$c_{l\alpha}$	2π
$c_{l\delta}$	1
c_{d0}	0.01
c_{m0}	0.025
$c_{m\delta}$	−0.25
Aerodynamic coefficients for pods (about 25% chord)	
$c_{l\alpha}$	5
c_{d0}	0.02
c_{m0}	0

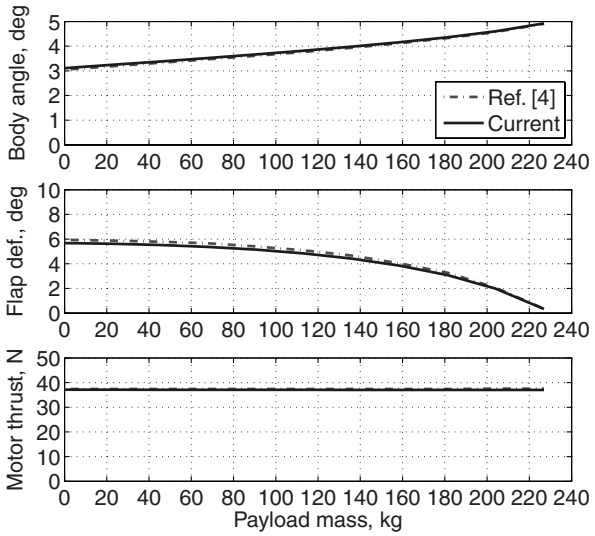

Fig. 12 Trim results for the flying wing vehicle.

variables are grouped together, leading to the linearized system of equations. Details about the linearization process can be found in [16]. Table 3 summarizes the results for the two extreme loading conditions: light and heavy, including the results given in [4]. Significant differences are present for both phugoid and short-period modes. The latter is never oscillatory in the present model. Figure 15 shows the phugoid mode of the vehicle from light to heavy configuration, with the comparison between the flexible vehicle and the one with only rigid-body degrees of freedom. With the increase of payload, the frequency of the phugoid mode grows, while the damping decreases. At 152 kg payload, the root locus of the flexible vehicle crosses the imaginary axis, which indicates the phugoid mode loses its stability. Qualitatively, the result is the same as reported in [4]. The quantitative differences are attributed mainly to differences in the aerodynamic damping and inertia between the two models, since the steady aerodynamic loads are virtually the same between [4] and the present work.

Still following correlations with results presented in [4], a nonlinear time simulation on the vehicle response is performed. The heavy flying wing configuration is initially at the trimmed condition. Perturbation is introduced by a commanded flap angle change: between 1 and 2 s, the flap angle is linearly ramped up to 5 deg, and it is linearly ramped back to its trimmed angle between 2 and 3 s.

As introduced, there are two stall models considered in the study. For both the stall models, the stall angle is 14 deg and the constant lift coefficient $c_{l_{\max}}$ is 1.54 when the stall angle is reached. In stall model 2, the moment coefficient is dropped from 0.025 to −0.02 once the angle of attack goes beyond the stall angle.

Table 2 Trim results for light and heavy configurations

	Body angle, deg	Flap angle, deg	Thrust per motor, N
Light	3.1	5.7	37
Heavy	4.9	0.3	37

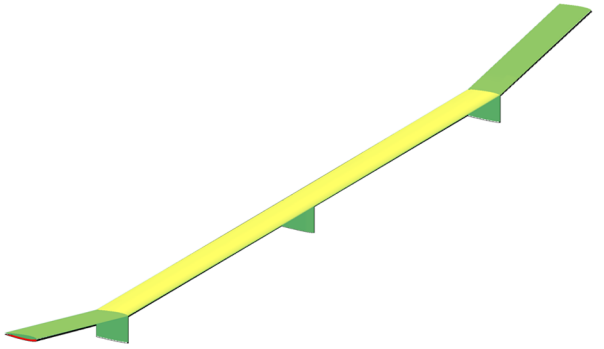

Fig. 13 Trimmed light model with respect to undeformed shape: nearly identical; $U = 12.2$ m/s at sea level.

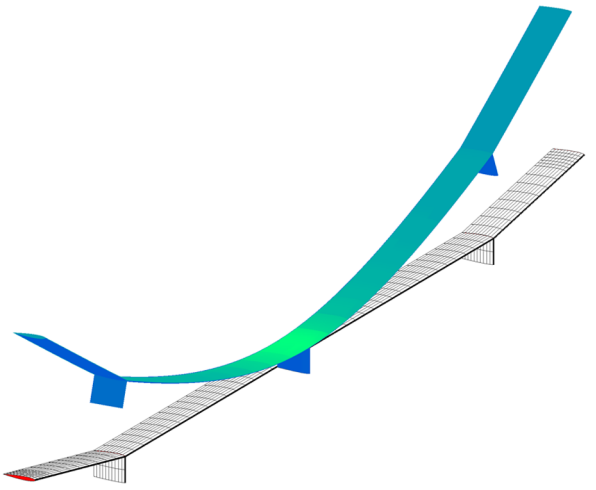

Fig. 14 Trimmed heavy model with respect to undeformed shape; $U = 12.2$ m/s at sea level.

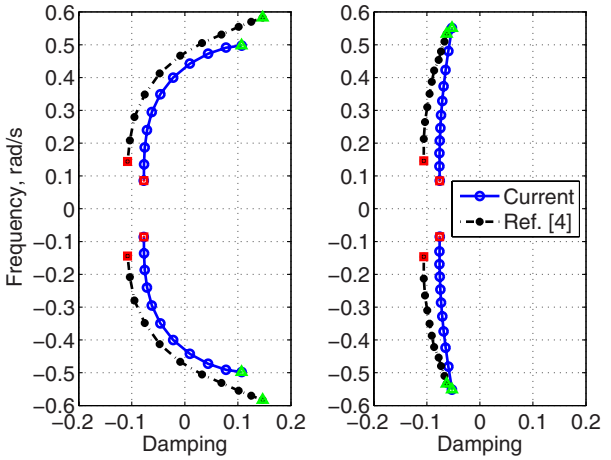

Fig. 15 Root locus for phugoid mode of the flying wing; payload from 0 (square) to 227 kg (triangle) (left: flexible vehicle, right: rigid vehicle).

Table 3 Phugoid and short-period modes for light and heavy configurations

	Flexible		Rigid	
Mode	Phugoid	Short period	Phugoid	Short period
Light [4]	$-0.108 \pm 0.142i$	$-2.74 \pm 1.76i$	$-0.106 \pm 0.146i$	$-2.82 \pm 1.82i$
Light (current)	$-0.0771 \pm 0.0858i$	$-11.7/-8.28$	$-0.0758 \pm 0.0853i$	$-11.7/-8.54$
Heavy [4]	$+0.147 \pm 0.586i$	——	$-0.0613 \pm 0.535i$	$-3.05 \pm 1.63i$
Heavy (current)	$+0.107 \pm 0.498i$	$-7.53/-0.91$	$-0.0525 \pm 0.551i$	$-9.31/-6.13$

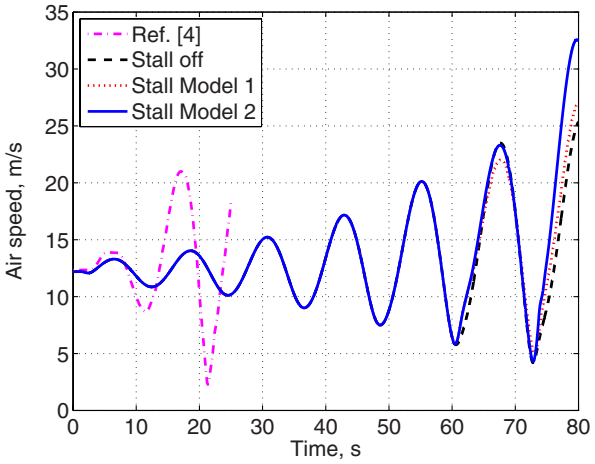

Fig. 16 Stall effects on the airspeed of flight with initial flap angle perturbation.

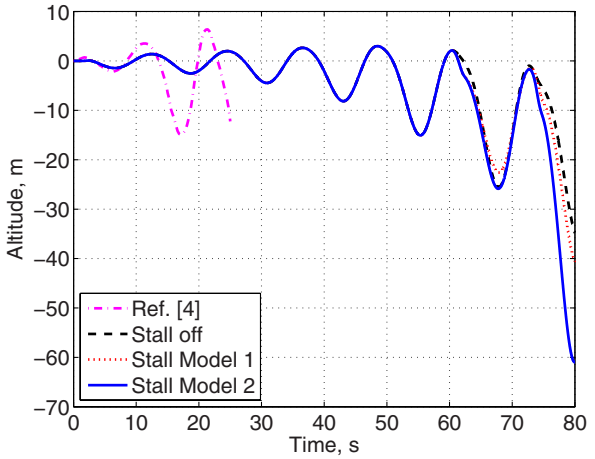

Fig. 17 Stall effects on the altitude of flight with initial flap angle perturbation.

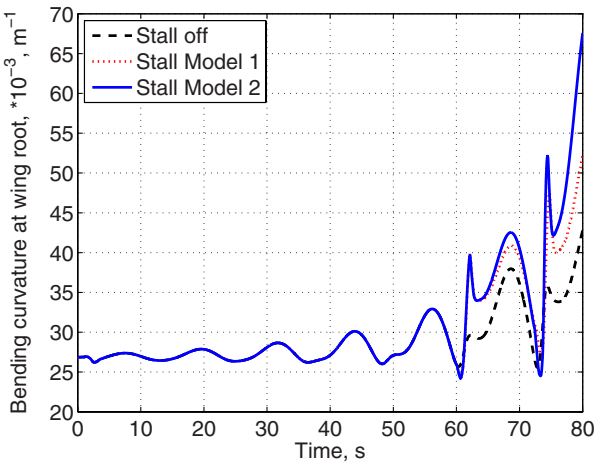

Fig. 19 Bending curvature at the midspan location of flight with initial flap angle perturbation.

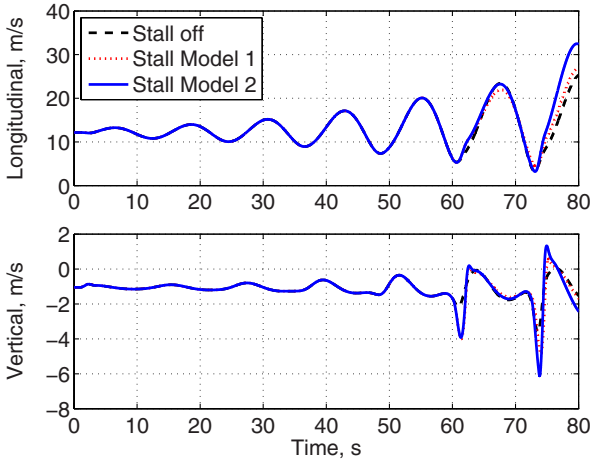

Fig. 20 Variation of body velocities with initial flap angle perturbation.

Figures 16–20 show the flying wing response for the first 80 s. Figures 16 and 17 show the variation of airspeed and altitude of the vehicle, including the two stall models, no stall effects, and the results presented in [4] for similar perturbation. As already discussed, the model used in [4] and the one in the present study feature different damping (and frequency to a lesser extent). In addition, [4] did not consider any stall effects. From those two figures, the exchange between kinetic energy and potential energy of the vehicle is seen through the out-of-phase variation between air speed and altitude. The unstable phugoid mode makes the oscillations grow with time for the heavy vehicle configuration.

As shown in Fig. 18, the midspan location (root) angle of attack reaches the stall angle within a few cycles. From Fig. 18, one may also see the difference of the angle of attack, with and without stall effects. While this shows stall at the midspan section of the flying wing happening at around 60 s, the wing tip starts experiencing stall about 0.5 s earlier. Among the things that can be observed from this

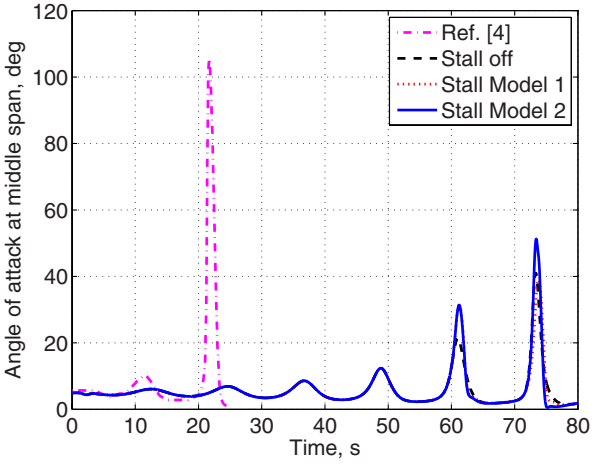

Fig. 18 Stall effects on the angle of attack of flight with initial flap angle perturbation.

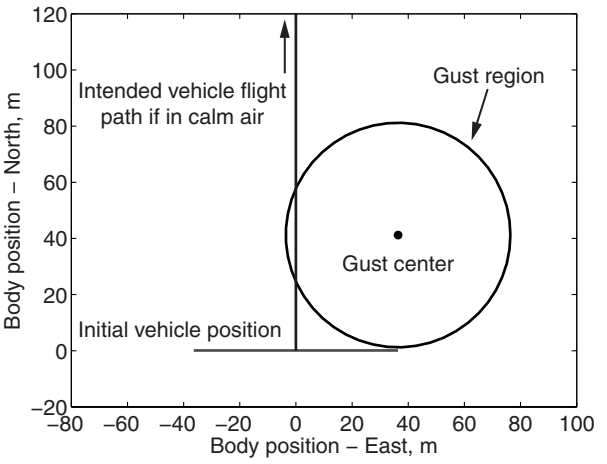

Fig. 21 Initial vehicle position with respect to the gust region and the intended vehicle flight path if in calm air.

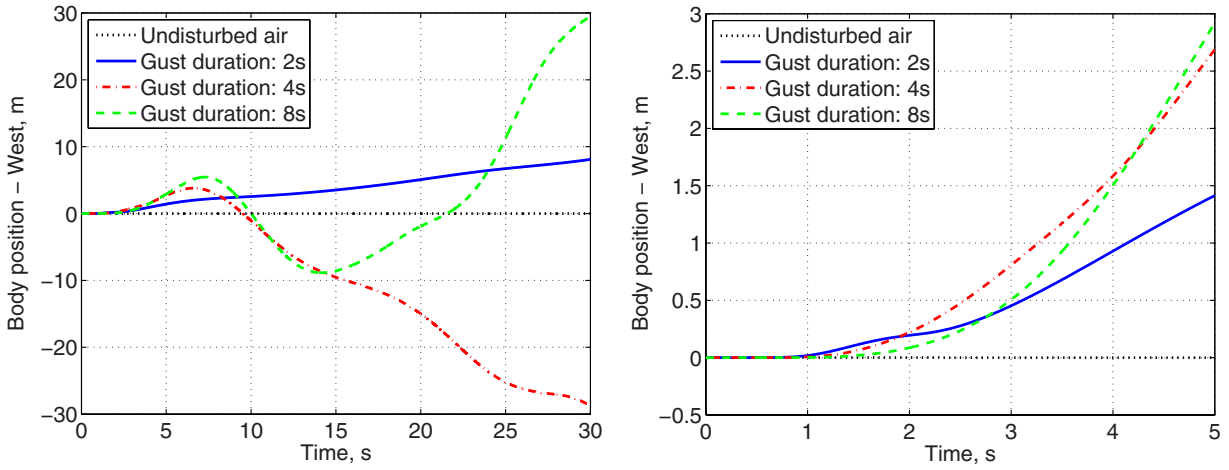

a) Time range: 0 – 30 s **b) Time range: 0 – 5 s**

Fig. 22 Effects of gust duration on *B* frame lateral position.

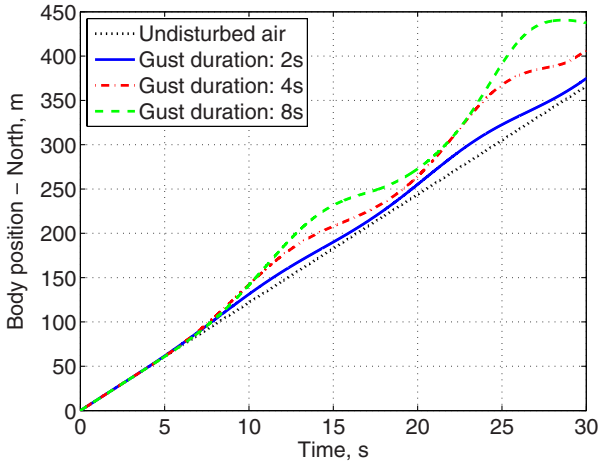

Fig. 23 Effects of gust duration on *B* frame longitudinal position.

series of results is that, at certain points, a higher angle of attack is obtained with stall effects on than with stall effects off. This is due to the difference between aerodynamic loads before and after the onset of stall. Once the stall angle is approached, the fixed level of aerodynamic lift load results in insufficient force to balance the vehicle weight, in contrast to a continuous linear increase of lift with static angle of attack when stall is off. Therefore, the altitude of the vehicle reduces with increased vertical velocity (Fig. 20), leading to

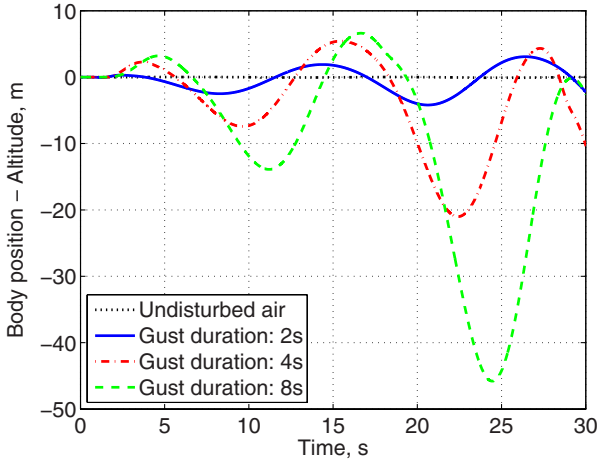

Fig. 24 Effects of gust duration on *B* frame altitude.

instantaneous higher angles of attack. However, the lift reduces the descent rate, and the angle of attack falls back to be smaller than the stall angle. This cycle repeats, and an oscillation in body vertical velocity can be observed. For the simulation with stall model 2, the sudden reduction in aerodynamic moment when the stall angle is reached accentuates this behavior. The corresponding change in body velocities is larger than the one with stall model 1. Since the actual stall characteristics of an airfoil will depend on the specific vehicle application (not defined in this work) and, qualitatively, the two stall models studied here give similar results, only stall model 2 will be applied in the results to follow.

D. Gust Response

As already discussed, the flying wing vehicle studied here in its heavy configuration shows a very large deformation under level flight. This large deformation may lead to flight dynamic instability and may compromise the vehicle's structural integrity under gust excitations.

To better understand the vehicle response under gust conditions, the discrete gust model described previously is used. The maximum gust amplitude at the center of the gust region A_c is 10 m/s. The spatial distribution within the gust region is given by Eqs. (15) and (16) with the following parameters: $r_0 = 40$ m, $n_N = 2$, and $n_E = 1$. The gust duration t_g can be 2, 4, or 8 s. Figure 21 shows the initial vehicle position ($t = 0$ s) with respect to the gust profile and its intended flight path, if in calm air. Note that the nominal flight speed is 12.2 m/s at sea level, and the right wing of the vehicle begins to touch the gust region after 0.1 s.

With stall model 2 applied, the aerodynamic lift force stops increasing with the angle of attack when the stall angle is reached, and the constant component of the aerodynamic pitch moment is reversed, making the airfoil pitch down. Figures 22–24 show the body positions of the vehicle with gust perturbations for the three different gust durations. The first observation from these plots is that the vehicle flies away from the gust center after it penetrates the gust region (up to 3.5 s). The gust may increase the airfoil plunging motion velocity [in Eq. (13)], which results in increased local lift forces. Since the gust distribution on the vehicle is not symmetric, roll and yaw moments about the vehicle's center of gravity are generated, which leads to roll and yaw motions. For the initial stages when the vehicle penetrates the gust region (before 2.0 s), the lateral deviation is not increased with the increase of the gust duration (Fig. 22b). This is because the longer gust duration introduces a smaller loading gradient on the wing, leading to smaller trajectory deviations at the beginning. However, the longer exposure will supply more energy to the motion, and the deviation from the intended trajectory (within calm air) will surpass the ones from shorter gust durations. The flight path, however, may change its direction due to different gust

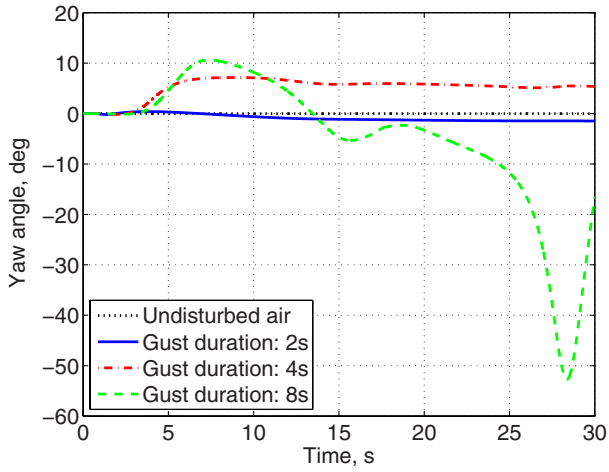

a) Time range: 0 – 30 s

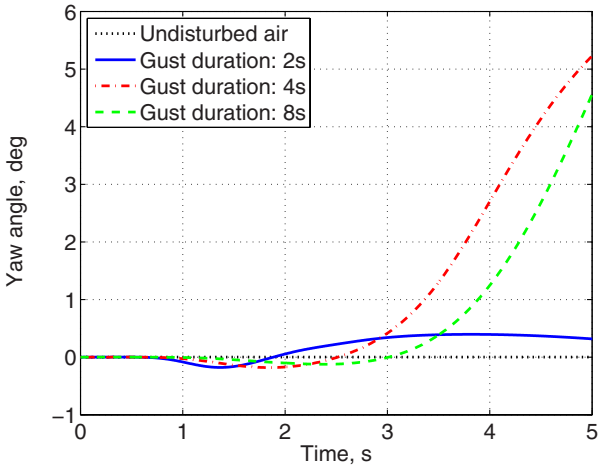

b) Time range: 0 – 5 s

Fig. 25 Effects of gust duration on *B* frame yaw angle.

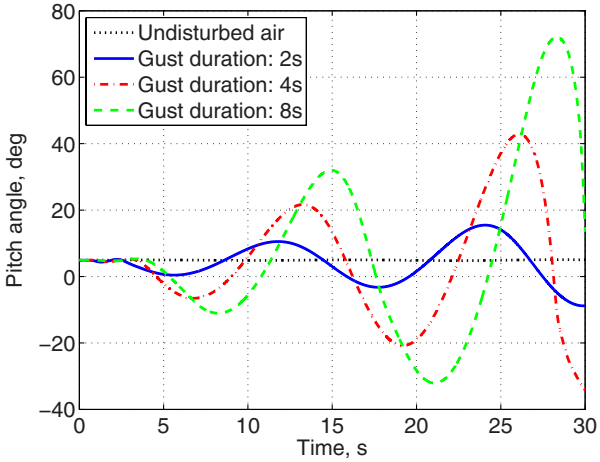

Fig. 26 Effects of gust duration on *B* frame pitch angle.

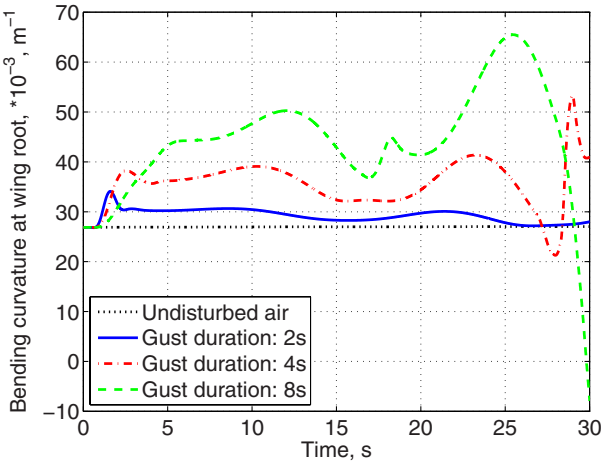

Fig. 28 Effects of gust duration on midspan bending curvature.

durations, as one can observe from Fig. 22. For the cases with 4 and 8 s gusts, the flight path heads back to the gust side after 6 to 7 s, while the 2 s gust case demonstrates unchanged deviation direction. This is due to the oscillation of the wings after the gust perturbation ceases. For the 4 and 8 s cases, the right wings bend down when the gust effects disappear, which leads to a downward local plunging motion velocity [in Eq. (13)]. Therefore, the local lift forces and moments on the right wing become lower than the left one, resulting in a positive yaw moment about the vehicle's center of gravity. On the other hand, the 2 s gust applies relatively little energy to the wings, such that the downward motion of the right wing does not generate enough yaw moment to overcome the ongoing vehicle motion. Moreover, the vehicle motion of the 8 s case is more complicated, since the oscillation of the right wing may lead to another change of the yaw

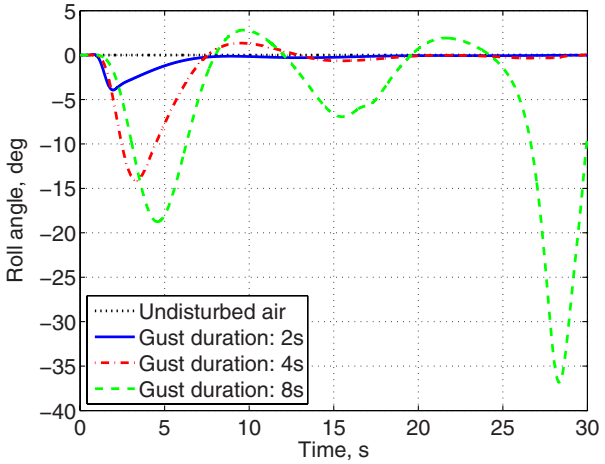

Fig. 27 Effects of gust duration on *B* frame roll angle.

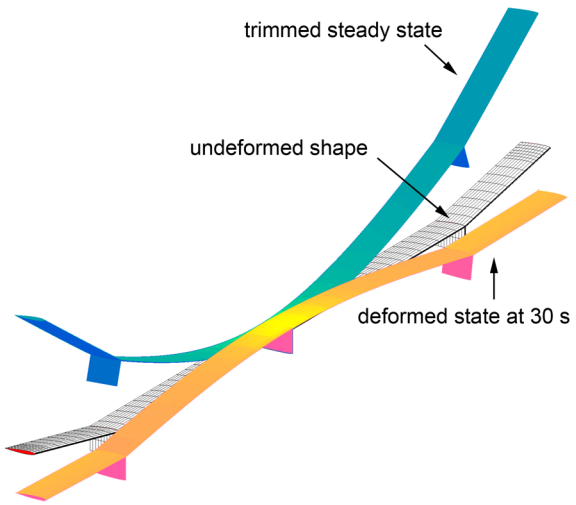

Fig. 29 Vehicle deformation shape at 30 s after encountering the 8 s gust disturbance.

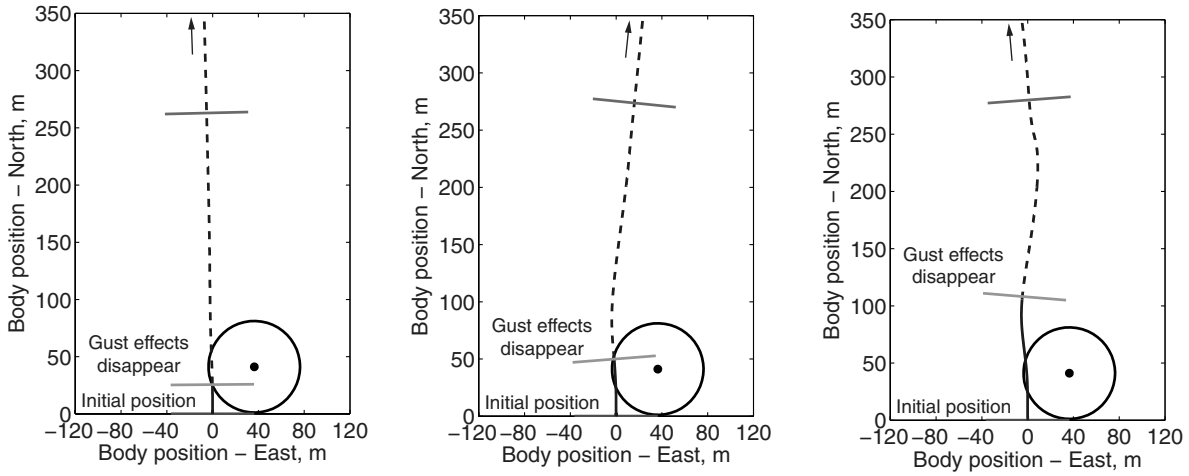

a) Gust duration: 2 s b) Gust duration: 4 s c) Gust duration: 8 s

Fig. 30 Flight path of the flying wing with different gust durations.

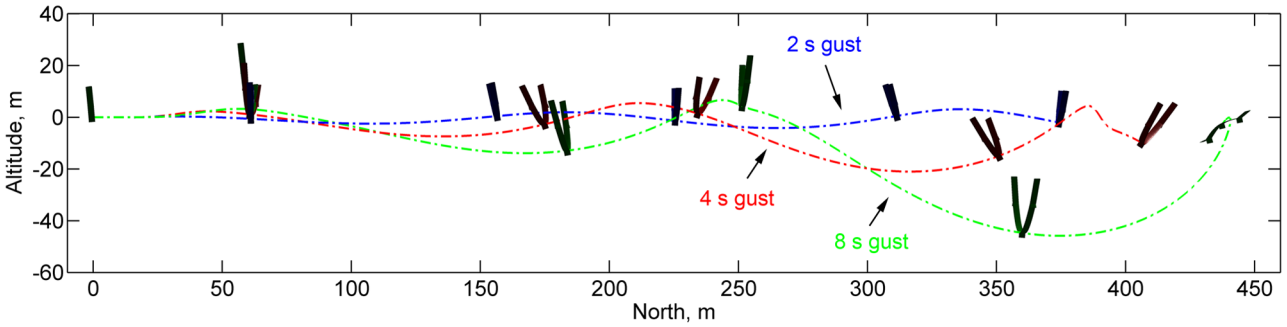

Fig. 31 Instantaneous positions and orientations of the flying wing with different gust durations.

direction after 15 s. After all, it is also noticeable that the amplitude of the plunging motion is increased with time, as shown in Fig. 24. This is the result of the vehicle's phugoid mode being unstable.

Figures 25–27 describe the changes in the Euler angles of the body frame as the vehicle goes through the gust perturbation. The variation of the yaw angle has a similar tendency to the body positions. If one looks at the details of the yaw angle at early stages of flight (Fig. 25b), it is evident that, initially, the vehicle yaws away from the gust center but, subsequently, it yaws back into the gust. This is believed to be associated with adverse yaw due to decrease in lift on the right wing. It can also be seen from Fig. 26 that the pitch angle oscillates with increased amplitude, which indicates again a longitudinal unstable configuration. As for the roll angle, the 2 s gust duration is short enough that it tends to recover to its undisturbed value within the time window shown in Fig. 27. This is expected for a damped roll oscillation, since the lift distribution on the vehicle should return to its original one after the gust effects disappear. However, this symmetry of lift distribution cannot be seen for the 8 s gust. The local angles of attack at the two tips are still different, and the amplitude of the motion seems to still be growing. Longer simulation times would be required for the long-duration gust cases.

One more observation that can be made is on the wing deformation. Figure 28 compares the midspan bending curvature for the three cases. As seen, the vehicle experiences large bending deformation after 25 s, especially for the 8 s gust case. Figure 29 exemplifies the significant change in vehicle shape at the end of 30 s, under the 8 s gust disturbance. Significant difference can be observed between the deformations at 30 s and the trimmed steady state.

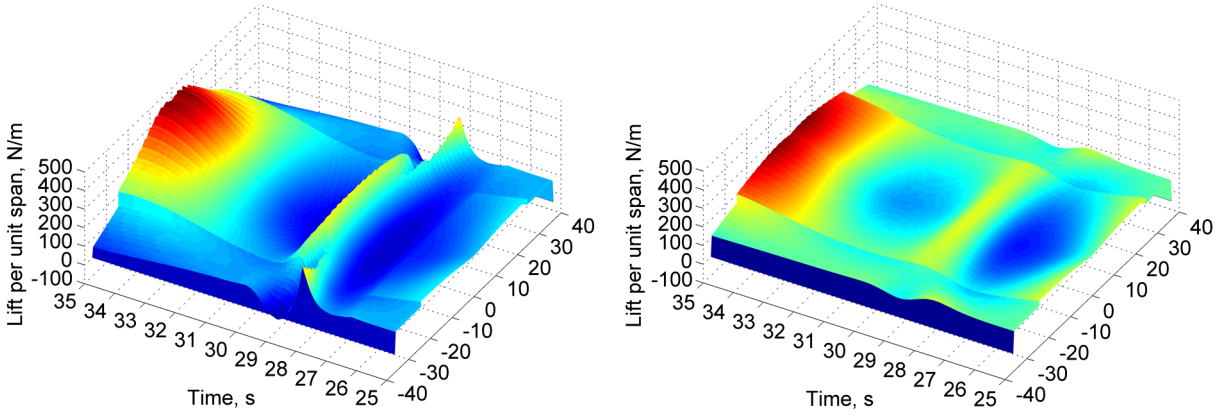

a) With stall effects b) Without stall effects

Fig. 32 Lift distribution on the wings from 25 to 35 s.

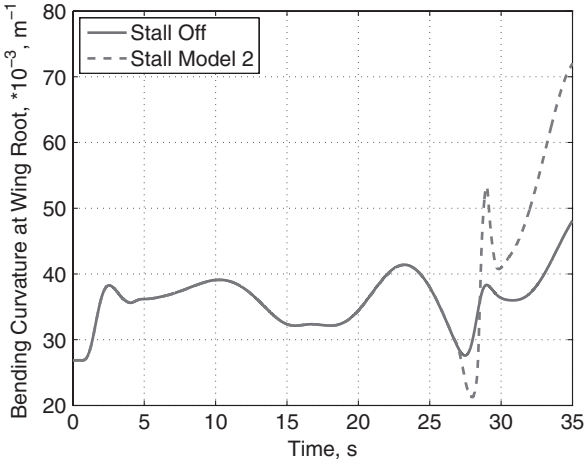

Fig. 33 Stall effects on midspan bending curvature (gust center amplitude: 10 m/s; duration: 4 s).

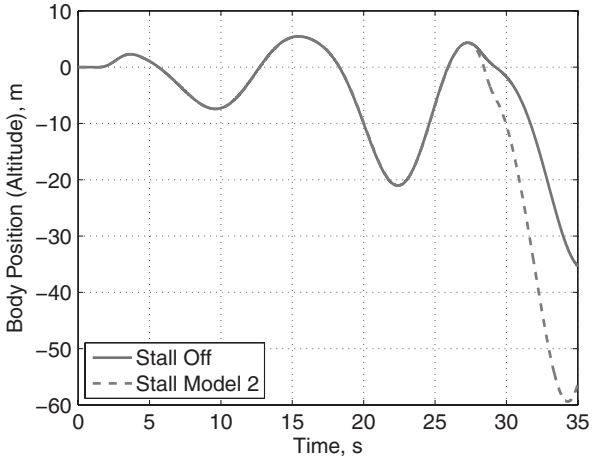

Fig. 36 Stall effects on *B* frame altitude (gust center amplitude: 10 m/s; duration: 4 s).

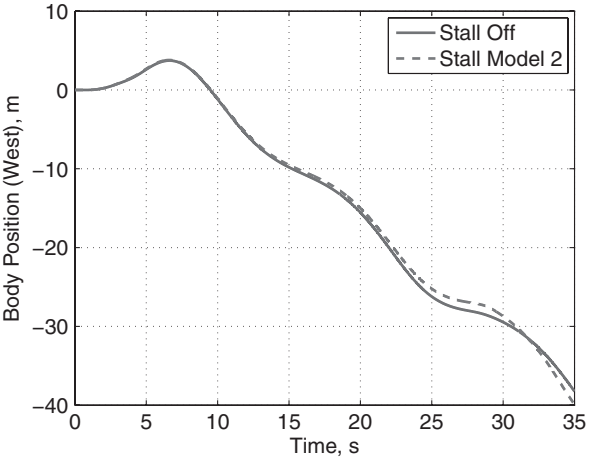

Fig. 34 Stall effects on *B* frame lateral position (gust center amplitude: 10 m/s; duration: 4 s).

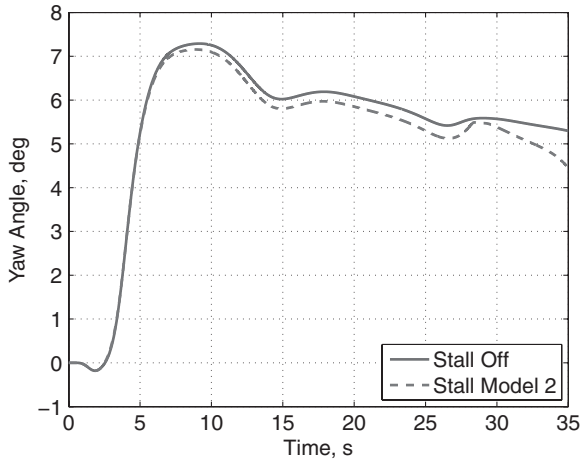

Fig. 37 Stall effects on *B* frame yaw angle (gust center amplitude: 10 m/s; duration: 4 s).

Figure 30 shows the flight path for the three different gust durations from a top view. For all cases, the initial position of the vehicle is represented at the bottom center position ($t = 0$ s). Since the gust cases have different durations, their ending point is also indicated in the figures by an appropriate label ("gust effects disappear"). After gust effects disappear, the trajectory of the vehicle is shown with a dashed line. The upper line normal to the trajectory indicates the vehicle position at 20 s. From here, one can see the different positions and orientations of the vehicle when it flies in the calm air after gust effects disappear. Figure 31 illustrates the instantaneous vehicle positions and orientations of the flying wing at the times of 0, 5, 12, 18, 24, and 30 s. The unstable phugoid motion can be clearly observed.

Another interesting observation can be made when the results after 25 s are examined. The response does not follow the same tendency as that before then. This is because, at approximately 25 s, the

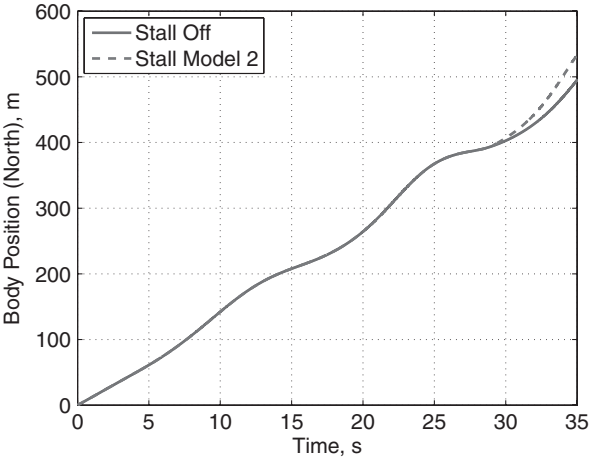

Fig. 35 Stall effects on *B* frame longitudinal position (gust center amplitude: 10 m/s; duration: 4 s).

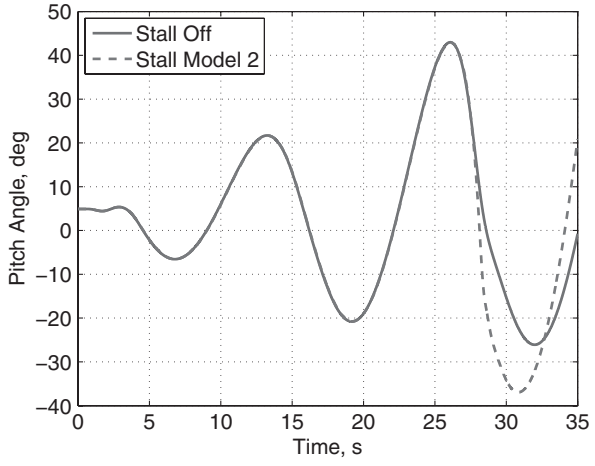

Fig. 38 Stall effects on *B* frame pitch angle (gust center amplitude: 10 m/s; duration: 4 s).

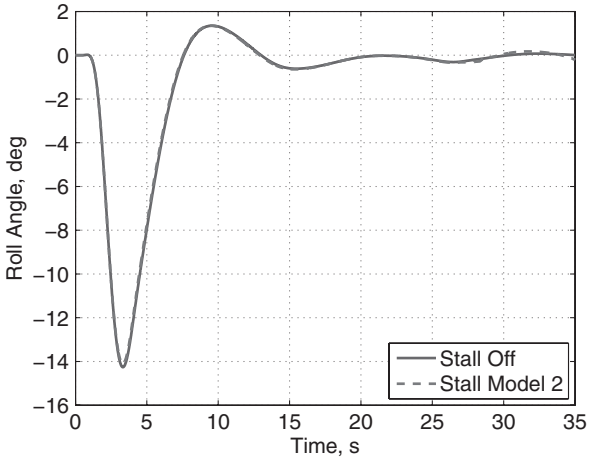

Fig. 39 Stall effects on *B* frame roll angle (gust center amplitude: 10 m/s; duration: 4 s).

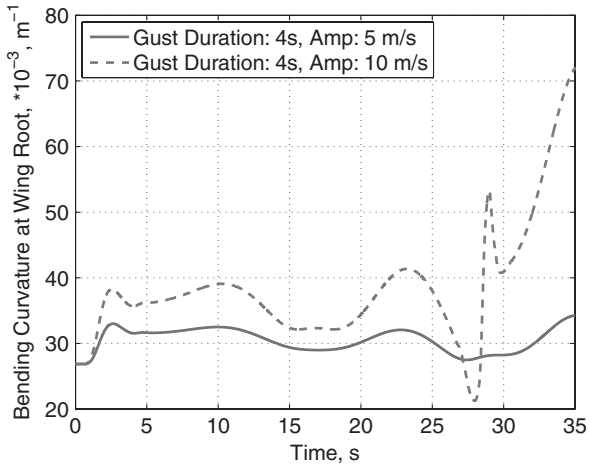

Fig. 40 Effects of gust amplitude on midspan bending curvature.

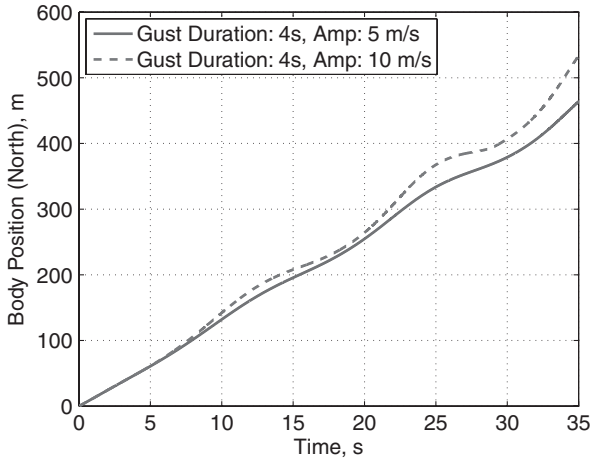

Fig. 42 Effects of gust amplitude on *B* frame longitudinal position.

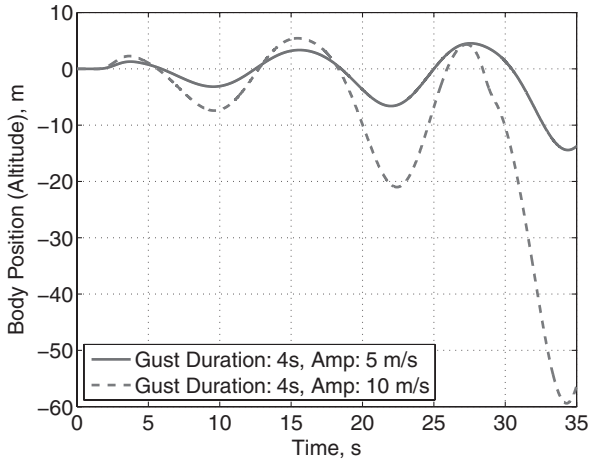

Fig. 43 Effects of gust amplitude on *B* frame altitude.

different wing stations exceed the stall angle of attack, changing the vehicle response. The effects of stall on the vehicle can be assessed by turning off the stall effects and comparing the results with and without stall effects. Only the 10 m/s center amplitude and 4 s duration gust case are analyzed. Results are presented for vehicle responses considering stall on and stall off. With stall effects turned on, the aerodynamic loads on the airfoil are not continuous before and after the moment of stall (Fig. 32). The discontinuity results in reductions in loads and the corresponding midspan bending curvature, as shown in Fig. 33. Although there is a sudden drop in lift at around 28 s, the transient loads excite the vehicle to large deformations and, eventually, large root strains. The configuration has an unstable phugoid mode that exacerbates the transient response and reaches higher bending curvatures levels. The impact of stall on vehicle response is illustrated in Figs. 34–39. The difference after 28 s can be clearly seen from those plots, where stall leads to an increase in plunging motion (Fig. 36) and pitch angle (Fig. 38). Therefore, stall effects can have a significant impact on the trajectory and attitude predictions.

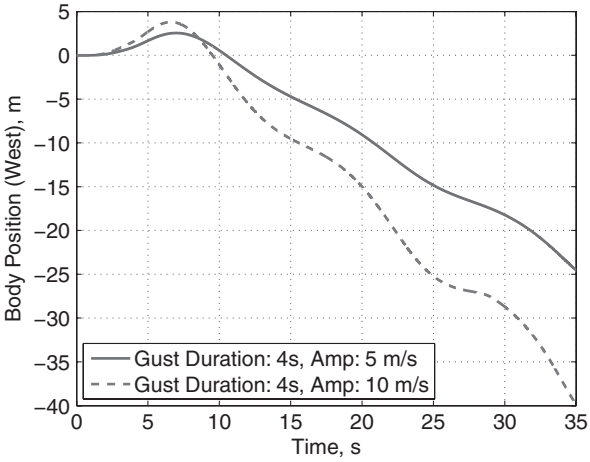

Fig. 41 Effects of gust amplitude on *B* frame lateral position.

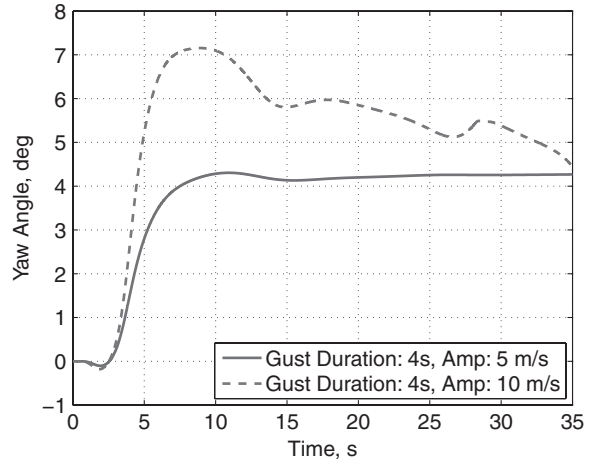

Fig. 44 Effects of gust amplitude on *B* frame yaw angle.

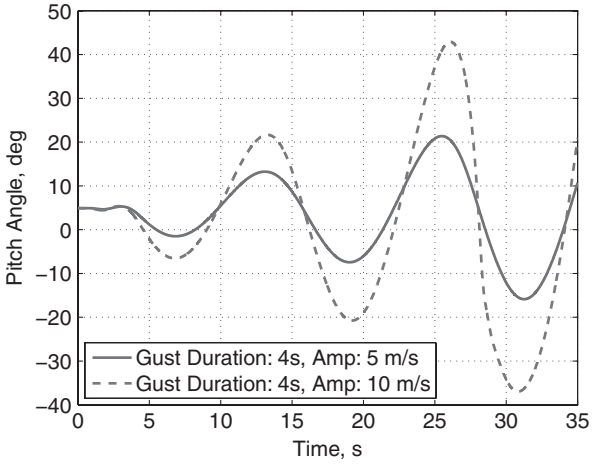

Fig. 45 Effects of gust amplitude on *B* frame pitch angle.

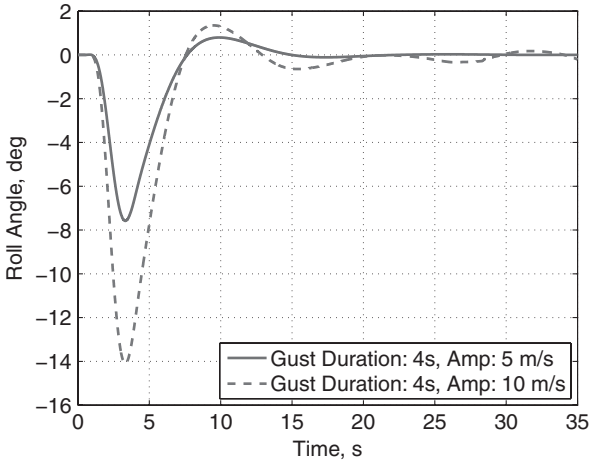

Fig. 46 Effects of gust amplitude on *B* frame roll angle.

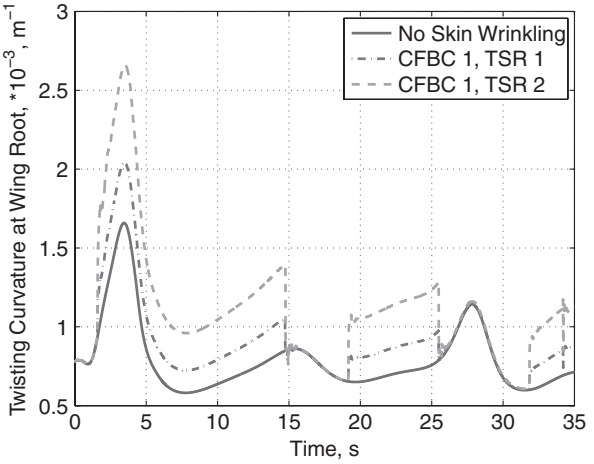

Fig. 48 Effects of skin wrinkling on midspan twist curvature (gust center amplitude: 5 m/s; duration 4 s).

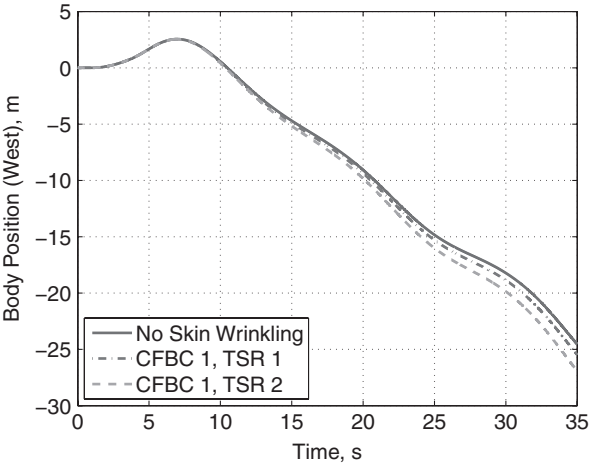

Fig. 49 Effects of skin wrinkling on *B* frame lateral position (gust center amplitude: 5 m/s; duration 4 s).

It is expected that different gust amplitudes will have different effects on the vehicle response. In the present study, a similar gust perturbation with maximum center amplitude of 5 m/s is applied, and the results are compared with the 10 m/s gust, as used previously. Note that both of the gust disturbances have the same duration of 4 s. Figure 40 presents the comparison of bending curvature at the vehicle midspan station. It shows that the two cases have similar responses before 25 s, with values directly proportional to the gust magnitude. However, the bending curvature of the 5 m/s gust response shows a more regular pattern up to 35 s, while the 10 m/s gust response shows an increase in bending curvature after an initial sudden reduction right after 25 s. This variation is related with stall effects, as discussed previously. However, the absence of the sudden reduction in the 5 m/s gust case does not mean there will not be any stall happening. Figures 41–46 compare the body position

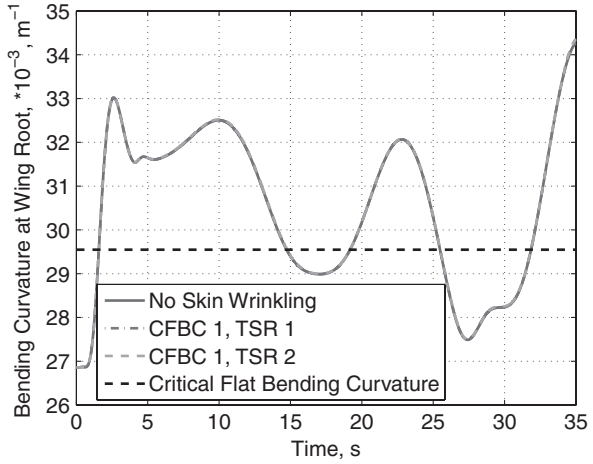

Fig. 47 Effects of skin wrinkling on midspan bending curvature (gust center amplitude: 5 m/s; duration 4 s).

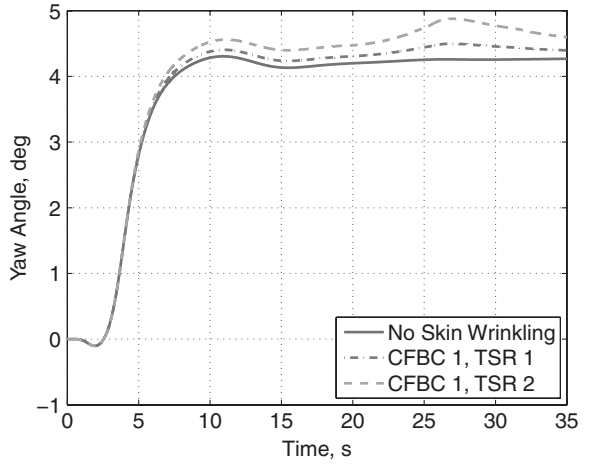

Fig. 50 Effects of skin wrinkling on *B* frame yaw angle (gust center amplitude: 5 m/s; duration 4 s).

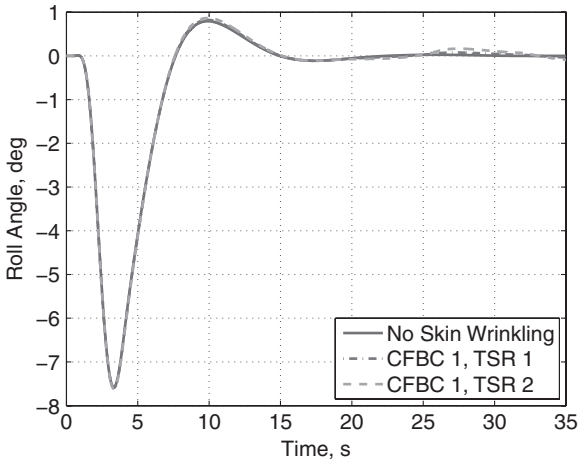

Fig. 51 Effects of skin wrinkling on *B* frame roll angle (gust center amplitude: 5 m/s; duration 4 s).

and orientation of the vehicle under gust perturbations with different amplitudes. Since the phugoid mode of the vehicle is unstable, reinforced by the responses shown in Figs. 43 and 45, the angle of attack will eventually grow to reach stall, and a similar outcome to the 10 m/s gust response is anticipated.

E. Effects of Skin Wrinkling on Gust Response

In this section, the effects of skin wrinkling on the gust response are investigated. From preliminary simulations, the region most likely to reach higher curvature is located at the midspan (wing root). Postwrinkling torsional stiffness reductions are selected as 20% (denoted as TSR 1) and 40% (denoted as TSR 2) of the original one for this study (see Figs. 47 and 48). As discussed before, the threshold point between the two torsional stiffness states is determined by the corresponding flat bending curvature. The critical flat bending curvature is postulated to be 0.02955 m^{-1} (denoted as CFBC 1), which is 10% higher than the bending curvature of the fully loaded vehicle at level flight in calm air. Gust disturbance with 5 m/s center amplitude and 4 s duration is used. The flight speed is 12.2 m/s at sea level.

The bending and twist curvatures at the wing root are compared in Figs. 47 and 48, respectively. As one can see from the plots, the torsional stiffness changes accordingly when the threshold point of the bending curvature is reached, which results in the jump (up and down) of the twist curvature.

Figures 49–51 show some of the vehicle responses subject to wing skin wrinkling, with stall model 2 applied in the analysis. Skin wrinkling mainly affects the lateral motion and the yaw angle of the body. If the torsional stiffness reduces to 60% of nominal value when skin wrinkles, the difference of lateral displacement at the end of 35 s is about 2.38 m, which is about 9.71% of the lateral displacement when skin wrinkling is not considered. The corresponding difference in yaw angle is about 0.33 deg, which is approximately 7.71% of the yaw angle when skin wrinkling is not considered. For the other responses, the effects of skin wrinkling are very small.

IV. Conclusions

Dynamic response of highly flexible flying wings is inherently a nonlinear problem, which involves geometric and aerodynamic nonlinearities common in the aeroelastic analysis of highly flexible vehicles. Through a representative example case of this aircraft class, numerical studies were conducted to study the effects of flexibility, loading distribution, and gust disturbances. The study showed that finite gust disturbance could bring the flying wing to strong unstable divergence response. The role of aerodynamics, elastic/rigid motions, and their interactions under a variety of gust disturbances were detailed in the paper.

The nonlinear effects were addressed in this paper through a methodology that integrates all the necessary disciplines, including nonlinear strain-based beam model, unsteady aerodynamics with simplified stall models, and the six-degree-of-freedom flight dynamic formulation. These were implemented in the computer code UM/NAST. With it, fully nonlinear time-marching analyses were performed. The nonlinear equations were also linearized about given nonlinear equilibrium states, such that flight dynamic stability of the vehicle could be assessed. A spatially and temporally distributed discrete gust model was seamlessly integrated into the time-domain simulation to study the gust response of the Helios-like flying wings. The implementation is general to enable the formulation to accommodate other gust models in time-domain analysis. Finally, the skin wrinkling effects were modeled through a bilinear torsional stiffness representation.

A detailed study was conducted of the dynamic response of a representative highly flexible flying wing previously presented in the literature. Flight dynamic stability was analyzed at the trimmed conditions with different payloads. With an increase in payload at its center pod, the vehicle moved from a span-loaded to a center-loaded configuration. The trimmed shape was significantly different from the reference one, which in turn caused changes in the flight dynamic modes. The phugoid mode eventually became unstable with the increased payload and wing deformation. The short-period mode was not oscillatory for the range of payloads considered. Fully nonlinear time-domain simulation was performed with an initial flap perturbation from the trimmed condition. The unstable phugoid mode was clearly excited, which compromised the performance and, eventually, the integrity of the vehicle. In addition, the representative flying wing's response was analyzed for different gust amplitudes and durations. As expected, flight path, vehicle attitude, and structural motion were impacted by the presence of gust. The disturbed flight path may deviate from the gust center. However, the after-gust responses may develop differently with different initial gust durations, especially the flight path and the yaw angle. Furthermore, with the phugoid mode being unstable, a finite gust perturbation could result in uncontrollable diverging vehicle motions. The large plunging and pitching motions of the vehicle with corresponding large elastic deformations also resulted in high instantaneous angles of attack on some stations along the wing, which resulted in local stall. Physical discussions of the interaction among rigid- and flexible-body motions and stall effects were presented. The effects of stall had a significant impact on transient responses of the wing and could alter the vehicle flight behavior. Finally, the skin wrinkling associated with the wing torsional stiffness was shown to mainly affect the motions of the vehicle in the lateral direction. For the other responses, the effects of skin wrinkling were small based on the parameters chosen for the numerical study.

Acknowledgments

This work was partially supported by NASA Dryden Flight Research Center under contract NND05AC19P. The technical monitor was Martin J. Brenner. The views expressed in this article are those of the authors and do not reflect the official policy or position of NASA or the U.S. Government. The authors are also grateful to Christopher M. Shearer (U.S. Air Force) for his help with the flight dynamics in University of Michigan's Nonlinear Aeroelastic Simulation Toolbox.

References

[1] Patil, M. J., Hodges, D. H., and Cesnik, C. E. S., "Nonlinear Aeroelasticity and Flight Dynamics of High-Altitude Long-Endurance Aircraft," *Journal of Aircraft*, Vol. 38, No. 1, 2001, pp. 88–94. doi:10.2514/2.2738

[2] Patil, M. J., Hodges, D. H., and Cesnik, C. E. S., "Limit-Cycle Oscillations in High-Aspect-Ratio Wings," *Journal of Fluids and Structures*, Vol. 15, No. 1, 2001, pp. 107–132. doi:10.1006/jfls.2000.0329

[3] Noll, T. E., Brown, J. M., Perez-Davis, M. E., Ishmael, S. D., Tiffany, G. C., and Gaier, M., "Investigation of the Helios Prototype Aircraft

Mishap. Volume 1: Mishap Report" [online paper], 2004, http://www.nasa.gov/pdf/64317main_helios.pdf [retrieved 07 Aug. 2010].

[4] Patil, M. J., and Hodges, D. H., "Flight Dynamics of Highly Flexible Flying Wings," *Journal of Aircraft*, Vol. 43, No. 6, 2006, pp. 1790–1798.
doi:10.2514/1.17640

[5] Hoblit, F. M., *Gust Loads on Aircraft: Concepts and Applications*, AIAA Education Series, AIAA, Washington, DC, 1988, pp. 29–46.

[6] Patil, M. J., and Taylor, D. J., "Gust Response of Highly Flexible Aircraft," 47th AIAA/ASME/ASCE/AHS/ASC Structures, Structural Dynamics, and Materials Conference, Newport, RI, AIAA Paper 2006-1638, 1–4 May 2006.

[7] Patil, M. J., "Nonlinear Gust Response of Highly Flexible Aircraft," 48th AIAA/ASME/ASCE/AHS/ASC Structures, Structural Dynamics, and Materials Conference, Honolulu, HI, AIAA Paper 2007-2103, 23–26 April 2007.

[8] Love, M. H., Zink, P. S., Wieselmann, P. A., and Youngren, H., "Body Freedom Flutter of High Aspect Ratio Flying Wings," 46th AIAA/ASME/ASCE/AHS/ASC Structures, Structural Dynamics, and Materials Conference, Austin, TX, AIAA Paper 2005-1947, 18–21 April 2005.

[9] Raghavan, B., and Patil, M. J., "Flight Dynamics of High-Aspect-Ratio Flying Wings: Effect of Large Trim Deformation," *Journal of Aircraft*, Vol. 46, No. 5, 2009, pp. 1808–1812.
doi:10.2514/1.36847

[10] Shearer, C. M., and Cesnik, C. E. S., "Nonlinear Flight Dynamics of Very Flexible Aircraft," *Journal of Aircraft*, Vol. 44, No. 5, 2007, pp. 1528–1545.
doi:10.2514/1.27606

[11] Radcliffe, T. O., and Cesnik, C. E. S., "Aeroelastic Response of Multi-Segmented Hinged Wings," 42nd AIAA/ASME/ASCE/AHS/ASC Structures, Structural Dynamics, and Materials Conference and Exhibit, Seattle, WA, AIAA Paper 2001-1371, 16–19 April 2001.

[12] Hénon, M., "On the Numerical Computation of Poincaré Maps," *Physica D, Nonlinear Phenomena*, Vol. 5, Nos. 2–3, 1982, pp. 412–414.
doi:10.1016/0167-2789(82)90034-3

[13] Cesnik, C. E. S., and Brown, E. L., "Active Wing Warping Control of a Joined-Wing Airplane Configuration," 44th AIAA/ASME/ASCE/AHS/ASC Structures, Structural Dynamics, and Materials Conference, Norfolk, VA, AIAA Paper 2003-1715, 7–10 April 2003.

[14] Cesnik, C. E. S., and Su, W., "Nonlinear Aeroelastic Modeling and Analysis of Fully Flexible Aircraft," 46th AIAA/ASME/ASCE/AHS/ASC Structures, Structural Dynamics, and Materials Conference, Austin, TX, AIAA Paper 2005-2169, 18–21 April 2005.

[15] Cesnik, C. E. S., and Brown, E. L., "Modeling of High Aspect Ratio Active Flexible Wings for Roll Control," 43rd AIAA/ASME/ASCE/AHS/ASC Structures, Structural Dynamics, and Materials Conference, Denver, CO, AIAA Paper 2002-1719, 22–25 April 2002.

[16] Su, W., and Cesnik, C. E. S., "Nonlinear Aeroelasticity of a Very Flexible Blended-Wing-Body Aircraft," *Journal of Aircraft*, Vol. 47, No. 5, 2010, pp. 1539–1553.
doi:10.2514/1.47317

[17] Peters, D. A., and Johnson, M. J., "Finite-State Airloads for Deformable Airfoils on Fixed and Rotating Wings," *Proceedings of Symposium on Aeroelasticity and Fluid Structure Interaction Problems, ASME Winter Annual Meeting*, edited by P. P. Friedmann and J. C. I. Chang, AD-Vol. 44, American Soc. of Mechanical Engineers, New York, 1994, pp. 1–28.

E. Livne
Associate Editor